Elastic relaxations associated with the $Pm\bar{3}m$–$R\bar{3}c$ transition in LaAlO$_3$: II. Mechanisms of static and dynamical softening

Elastic relaxations associated with the $Pm\bar{3}m$–$R\bar{3}c$ transition in LaAlO₃: II. Mechanisms of static and dynamical softening

M A Carpenter[1], S V Sinogeikin[2,3] and J D Bass[2]

[1] Department of Earth Sciences, University of Cambridge, Downing Street,
Cambridge CB2 3EQ, UK
[2] Department of Geology, University of Illinois, Urbana, IL 61801, USA

E-mail: mc43@esc.cam.ac.uk

Abstract
Brillouin spectra have been collected *in situ* at temperatures up to ∼1000 K for different
crystallographic directions from two single crystal plates of LaAlO₃ perovskite. Elastic moduli
derived from these, together with heat capacity, spontaneous strain and Raman data from the
literature, have then been used to calibrate the coefficients in a classical Landau free energy
expansion for the second order $Pm\bar{3}m \leftrightarrow R\bar{3}c$ phase transition at $T_c = 817$ K. The static
strain/order parameter coupling model provides a quantitative description of elastic softening
between room temperature and ∼700 K, but from ∼700 K up to T_c additional elastic softening
correlates with the development of a central peak in the Brillouin spectra. The presence of
quasi-elastic scattering, which reaches maximum intensity ∼5–15 K below T_c, implies a strong
dynamical component to the phase transition. Relaxation times estimated from the width of the
central peak are of the order of ∼10–100 ps and appear to be more or less constant between
∼700 and 800 K, which is consistent with an intrinsic origin associated with phonon density
fluctuations. Central peak width variations and an irregular pattern of acoustic velocity
variations in a 20 K temperature interval below T_c are interpreted in terms of flipping of clusters
of tilted octahedra between different $\langle 111 \rangle$, $\langle 011 \rangle$ and $\langle 001 \rangle$ tilt axes. The additional softening
beyond that expected from the classical strain/order parameter coupling model can be
understood in terms of coupling of acoustic modes with the central peak mode(s).

(Some figures in this article are in colour only in the electronic version)

1. Introduction

Any rigorous model of a phase transition must reproduce
the correct evolution of properties such as the equilibrium
order parameter and spontaneous strain, which depend on
first derivatives of free energy, and of properties such as soft
mode frequencies and elastic moduli, which depend on second
derivatives. In other words the model must reproduce not only
the location of minima in the free energy potential but also
its shape around those minima. This applies particularly to
the temperature (or pressure) interval close to the transition
point that tends to be the subject of argument in relation to
the validity of mean field models or renormalization group
theory. The $Pm\bar{3}m \leftrightarrow I4/mcm$ transition in SrTiO₃ at
∼106 K has probably been the most intensively scrutinized
of all phase transitions in this context, with contrasting views
summarized by Cowley (1996) and Salje *et al* (1998). The
general expectation is that a mean field description should
be valid over a wide temperature interval but that close to
the transition point the influence of fluctuations will become
significant. A recent review of most of the data in the literature
for stress, strain, elasticity and susceptibility for the 106 K

[3] Present address: HPCAT, Carnegie Institution of Washington, Argonne,
Illinois 60439, USA.

transition in $SrTiO_3$ has revealed that, while most of the observed behaviour conforms quantitatively to the solutions of a Landau expansion to sixth order in the order parameter (at least up to within a few degrees of the transition point), details of the soft mode evolution require only second and fourth order terms (Carpenter 2007). Thus, even in the case of such a well-studied system, it appears that behaviour away from the Ginsburg interval (where critical fluctuations develop) is not fully understood.

Another transition which has been investigated intensively over the years is the $Pm\bar{3}m \leftrightarrow R\bar{3}c$ transition in $LaAlO_3$ (Geller and Bala 1956, Cochran and Zia 1968, Müller *et al* 1968, Axe *et al* 1969, Scott 1969, Pytte and Feder 1969, Feder and Pytte 1970, Geller and Raccah 1970, Kjems *et al* 1973, O'Bryan *et al* 1990, Bueble *et al* 1998, Chrosch and Salje 1999, Chakoumakos *et al* 1998, Lehnert *et al* 2000, Howard *et al* 2000, Bouvier and Kreisel 2002, Hayward *et al* 2002, 2005, Harrison and Redfern 2002, Zhao *et al* 2004, Harrison *et al* 2004b, 2004a, Tohei *et al* 2005). In principle this occurs by the same R-point soft mode mechanism that applies for the $Pm\bar{3}m \leftrightarrow I4/mcm$ transition in $SrTiO_3$. An important difference, however, is that the transition occurs at a much higher temperature ($T_c \approx 820$ K). This means that, if deviations from classical second order character are observed, it should be much easier to account unambiguously for the separate contributions of saturation effects and high order terms than has been the case for $SrTiO_3$. The transition in $LaAlO_3$ also does not conform to straightforward solutions of a Landau free energy expansion in one order parameter, as shown by Hayward *et al* (2005) who identified anomalies in the evolution of soft mode frequencies, optical retardation, spontaneous strain, excess entropy, octahedral tilt angle and an internal structural distortion parameter between $\sim$720 K and T_c. They postulated that there is more than one order parameter in operation and, moreover, that this behaviour is common to La, Pr, Nd aluminate perovskites and $LaCoO_3$.

The present study was devised with the primary objective of characterizing the $Pm\bar{3}m \leftrightarrow R\bar{3}c$ transition in $LaAlO_3$ from the perspective of a second derivative property, namely elasticity. Following on from the determination of the elastic modulus tensor at room temperature (Carpenter *et al* 2010b), Brillouin scattering has been used to determine variations of the moduli in detail from room temperature to 1000 K. These are combined with additional data obtained by resonant ultrasound spectroscopy (RUS) at high temperatures (Carpenter *et al* 2010a). A fully calibrated Landau description has been developed in order to define the expected behaviour for a classical second order phase transition driven by a zone boundary soft mode. Deviations from this description show the extent to which the real behaviour is modified by other relaxational effects. The deviations, which increase in magnitude from $\sim$700 K towards T_c, correlate with the appearance of a quasi-elastic scattering central peak in the Brillouin spectra. Development of a Brillouin central peak of this type is commonly found to be associated with structural phase transitions, including the transition in $SrTiO_3$ (Lyons and Fleury 1977), and it can be due to a diversity of relaxation mechanisms (e.g., Fleury and Lyons 1979, 1981, 1983). As

far as the present authors are aware, however, a central peak associated with a transition which involves phases that are neither ferroelectric nor piezoelectric has not previously been observed to occur over such a wide temperature interval.

The paper is divided into 7 sections. Following this brief introduction, a full strain/order parameter coupling model is developed and all the Landau coefficients are calibrated using data from the literature or from the new elastic modulus measurements. Following a short section describing the experimental methods, results from measurements of $\sim$175 Brillouin spectra are presented. These were collected *in situ* at temperatures up to $\sim$1000 K and in different crystallographic directions within plates cut parallel to cubic (110) and (100). The analysis includes determination of elastic moduli and characterization of the evolution of the central peak. The spectrometer setup allowed the possibility of recording transmitted light images of the thin plates, so that it has been possible also to observe changes in the transformation twin microstructure through the transition and to correlate these with changes in the elastic properties. A full mode–mode coupling model is not included but deviations from the static Landau model are explained in terms of coupling of acoustic modes with the dynamic central peak mode in section 6. Contributions of phonon density fluctuations and a flip mode which causes reorientation of clusters of octahedra between different tilt axes are considered as possible causes of the quasi-elastic scattering. In the concluding section, the influence of the previously unidentified relaxational phenomena on other properties of $LaAlO_3$ are considered, together with the likelihood that the same effects might occur more widely in perovskite phase transitions at high temperatures.

2. Landau theory

Elastic anomalies associated with phase transitions can be described effectively using Landau theory. The appropriate free energy expansion, including coupling between components of the order parameter, q_1, q_2, q_3 and symmetry-adapted strains, e_a, e_o, e_t, e_4, for transitions from a $Pm\bar{3}m$ parent structure to structures with space groups related to the R point is (Carpenter *et al* 2001, Carpenter 2007)

$$
\begin{aligned}
G = {} & \frac{1}{2} a \Theta_s \left(\coth\left(\frac{\Theta_s}{T}\right) - \coth\left(\frac{\Theta_s}{T_c}\right) \right) \\
& \times (q_1^2 + q_2^2 + q_3^2) + \tfrac{1}{4}(q_1^2 + q_2^2 + q_3^2)^2 \\
& + \tfrac{1}{4} b'(q_1^4 + q_2^4 + q_3^4) + \lambda_1 e_a (q_1^2 + q_2^2 + q_3^2) \\
& + \lambda_2 [\sqrt{3} e_o (q_2^2 - q_3^2) + e_t (q_1^2 - q_2^2 - q_3^2)] \\
& + \lambda_3 (e_4 q_1 q_3 + e_5 q_1 q_2 + e_6 q_2 q_3) \\
& + \tfrac{1}{4}(C_{11}^o - C_{12}^o)(e_o^2 + e_t^2) + \tfrac{1}{6}(C_{11}^o + 2C_{12}^o)e_a^2 \\
& + \tfrac{1}{2} C_{44}^o (e_4^2 + e_5^2 + e_6^2).
\end{aligned}
\tag{1}
$$

Here a, b, b' are standard Landau coefficients, T_c is a critical temperature, λ_1, λ_2, λ_3 are coupling coefficients, Θ_s is the order parameter saturation temperature and C_{11}^o, C_{12}^o, C_{44}^o elastic moduli of the cubic structure, usually referred to as the bare elastic moduli. The symmetry-adapted strains are given by

$$
e_a = (e_1 + e_2 + e_3)
\tag{2}
$$

$$e_{\mathrm{o}} = (e_1 - e_2) \tag{3}$$

$$e_{\mathrm{t}} = \frac{1}{\sqrt{3}}(2e_3 - e_1 - e_2) \tag{4}$$

and e_4, e_5, e_6 are off-diagonal components of the strain tensor.

In the general case, relationships between strains and order parameter components are given by the equilibrium condition, $\partial G/\partial e = 0$ as

$$e_{\mathrm{a}} = -\frac{\lambda_1(q_1^2 + q_2^2 + q_3^2)}{\frac{1}{3}(C_{11}^{\mathrm{o}} + 2C_{12}^{\mathrm{o}})} \tag{5}$$

$$e_{\mathrm{o}} = -\frac{\lambda_2\sqrt{3}(q_2^2 - q_3^2)}{\frac{1}{2}(C_{11}^{\mathrm{o}} - C_{12}^{\mathrm{o}})} \tag{6}$$

$$e_{\mathrm{t}} = -\frac{\lambda_2(2q_1^2 - q_2^2 - q_3^2)}{\frac{1}{2}(C_{11}^{\mathrm{o}} - C_{12}^{\mathrm{o}})} \tag{7}$$

$$e_4 = -\frac{\lambda_3 q_1 q_3}{C_{44}^{\mathrm{o}}} \tag{8}$$

$$e_5 = -\frac{\lambda_3 q_1 q_2}{C_{44}^{\mathrm{o}}} \tag{9}$$

$$e_6 = -\frac{\lambda_3 q_2 q_3}{C_{44}^{\mathrm{o}}}. \tag{10}$$

Substituting these relationships back into equation (1) gives the renormalized form of the Landau expansion as

$$G = \frac{1}{2}a\Theta_{\mathrm{s}}\left(\coth\left(\frac{\Theta_{\mathrm{s}}}{T}\right) - \coth\left(\frac{\Theta_{\mathrm{s}}}{T_{\mathrm{c}}}\right)\right)(q_1^2 + q_2^2 + q_3^2)$$
$$+ \frac{1}{4}b^*(q_1^2 + q_2^2 + q_3^2)^2 + \frac{1}{4}b'^*(q_1^4 + q_2^4 + q_3^4) \tag{11}$$

where

$$b^* = b - \frac{\lambda_3^2}{C_{44}^{\mathrm{o}}} - \frac{2\lambda_1^2}{\frac{1}{3}(C_{11}^{\mathrm{o}} + 2C_{12}^{\mathrm{o}})} + \frac{4\lambda_2^2}{\frac{1}{2}(C_{11}^{\mathrm{o}} - C_{12}^{\mathrm{o}})} \tag{12}$$

$$b'^* = b' + \frac{\lambda_3^2}{C_{44}^{\mathrm{o}}} - \frac{12\lambda_2^2}{\frac{1}{2}(C_{11}^{\mathrm{o}} - C_{12}^{\mathrm{o}})}. \tag{13}$$

This compares with the form of the expansion used by Thomas and Müller (1968) and Harley *et al* (1973)

$$G = \frac{1}{2}A(T - T_{\mathrm{c}})(q_1^2 + q_2^2 + q_3^2) + \frac{1}{4}B(q_1^4 + q_2^4 + q_3^4)$$
$$+ \frac{1}{2}C(q_1^2 q_2^2 + q_2^2 q_3^2 + q_1^2 q_3^2), \tag{14}$$

where

$$B = b^* + b'^* = b + b' - \frac{2\lambda_1^2}{\frac{1}{3}(C_{11}^{\mathrm{o}} + 2C_{12}^{\mathrm{o}})} - \frac{8\lambda_2^2}{\frac{1}{2}(C_{11}^{\mathrm{o}} - C_{12}^{\mathrm{o}})} \tag{15}$$

$$C = b^* = b - \frac{\lambda_3^2}{C_{44}^{\mathrm{o}}} - \frac{2\lambda_1^2}{\frac{1}{3}(C_{11}^{\mathrm{o}} + 2C_{12}^{\mathrm{o}})} + \frac{4\lambda_2^2}{\frac{1}{2}(C_{11}^{\mathrm{o}} - C_{12}^{\mathrm{o}})}. \tag{16}$$

The rhombohedral ($R\bar{3}c$) structure has $q_1 = q_2 = q_3$, while other combinations of order parameter components give the subgroup symmetries listed in table 1. The stability fields of $I4/mcm$, $R\bar{3}c$ and $Imma$ structures depend on the sign and magnitude of B and C (e.g. see Thomas and Müller 1968, Harley *et al* 1973). In particular, for the part of parameter space where $B \approx C$, the $I4/mcm$ structure is stable when $B < C$ and the $R\bar{3}c$ structure is stable when $B > C$. This is

Table 1. Order parameter components for the subgroups of $Pm\bar{3}m$ associated with special point R_4^+ (after Howard and Stokes 1998). The system of reference axes for these components is that used in Stokes and Hatch (1988) and the group theory program ISOTROPY (http://stokes.byu.edu/isotropy.html).

Space group	Order parameter components	Relationships between order parameter components
$Pm\bar{3}m$	000	
$I4/mcm$	$q_1 00$	
$Imma$	$q_1 0 q_3$	$q_1 = q_3$
$R\bar{3}c$	$q_1 q_2 q_3$	$q_1 = q_2 = q_3$
$C2/m$	$q_1 0 q_3$	$q_1 \neq q_3$
$C2/c$	$q_1 q_2 q_3$	$q_1 = q_3 \neq q_2$
$P\bar{1}$	$q_1 q_2 q_3$	$q_1 \neq q_2 \neq q_3$

equivalent to the $I4/mcm$ or $R\bar{3}c$ structures being stable when b'^* is negative or positive, respectively. All three structures have the same energy when $B = C$. Thus the balance of stability below T_{c} is determined by the magnitudes of the terms in equation (13), including the coupling coefficients, λ_2 and λ_3, and the bare elastic moduli of the cubic parent structure. Strong coupling between the order parameter components and the e_4 strain (large $|\lambda_3|$) stabilizes the $R\bar{3}c$ structure, while strong coupling with e_{t} (large $|\lambda_2|$) stabilizes the $I4/mcm$ structure. Coupling with the volume strain, e_{a}, does not influence the relative stability of these two structures.

If the $Pm\bar{3}m \leftrightarrow R\bar{3}c$ transition is second order in character, the equilibrium variation of the order parameter as a function of temperature is given by (after Pérez-Mato and Salje 2001, Carpenter *et al* 2003)

$$q_1^2 = q_2^2 = q_3^2 = \frac{a\Theta_{\mathrm{s}}}{3b^* + b'^*}\left(\coth\left(\frac{\Theta_{\mathrm{s}}}{T_{\mathrm{c}}}\right) - \coth\left(\frac{\Theta_{\mathrm{s}}}{T}\right)\right)$$
$$= \frac{1}{3}\left(1 - \frac{\coth(\Theta_{\mathrm{s}}/T)}{\coth(\Theta_{\mathrm{s}}/T_{\mathrm{c}})}\right). \tag{17}$$

At 0 K, the value of $(q_1^2 + q_2^2 + q_3^2)$ including saturation, $(q_1^2 + q_2^2 + q_3^2)_{\mathrm{s}}$, with respect to $(q_1^2 + q_2^2 + q_3^2)$ without saturation, $(q_1^2 + q_2^2 + q_3^2)_{\mathrm{o}}$, becomes (from Salje *et al* 1991)

$$\frac{(q_1^2 + q_2^2 + q_3^2)_{\mathrm{s}}}{(q_1^2 + q_2^2 + q_3^2)_{\mathrm{o}}} = 1 - \tanh\left(\frac{\Theta_{\mathrm{s}}}{T_{\mathrm{c}}}\right) \tag{18}$$

where the value of $(q_1^2 + q_2^2 + q_3^2)_{\mathrm{o}}$ is usually set at 1.

In the vicinity of T_{c}, for $T_{\mathrm{c}} \gg \Theta_{\mathrm{s}}$, the excess heat capacity due to the transition is given by

$$\Delta C_{\mathrm{p}} = \frac{3a^2 T}{2(3b^* + b'^*)} = \frac{aT}{2T_{\mathrm{c}}}. \tag{19}$$

Note that,

$$3b^* + b'^* = 3b + b' - \frac{2\lambda_3^2}{C_{44}^{\mathrm{o}}} - \frac{6\lambda_1^2}{\frac{1}{3}(C_{11}^{\mathrm{o}} + 2C_{12}^{\mathrm{o}})} \tag{20}$$

and is independent of the coupling coefficient λ_2.

Application of a stress induces a strain which includes contributions from relaxation of the order parameter through the strain/order parameter coupling terms. Slonczewski and

Table 2. Elastic modulus variations expected in the stability field of a structure with $R\bar{3}c$ symmetry ($q_1 = q_2 = q_3$), due to a second order transition from a parent cubic structure with $Pm\bar{3}m$ symmetry (using reference axes for the cubic structure). Note that $\frac{1}{3}(C_{11} + 2C_{12})$ gives the Voigt value of the bulk modulus.

$$C_{11} = C_{22} = C_{33} = C_{11}^{o} - [4R_{11}(3\lambda_1^2 + 8\lambda_2^2) + 8R_{12}(3\lambda_1^2 - 4\lambda_2^2)]q_1^2$$

$$C_{12} = C_{13} = C_{23} = C_{12}^{o} - [4R_{11}(3\lambda_1^2 - 4\lambda_2^2) + 8R_{12}(3\lambda_1^2 + 2\lambda_2^2)]q_1^2$$

$$\tfrac{1}{2}(C_{11} - C_{12}) = \tfrac{1}{2}(C_{11}^{o} - C_{12}^{o}) - 24\lambda_2^2(R_{11} - R_{12})q_1^2$$

$$\tfrac{1}{3}(C_{11} + 2C_{12}) = \tfrac{1}{3}(C_{11}^{o} + 2C_{12}^{o}) - 12\lambda_1^2(R_{11} + 2R_{12})q_1^2$$

$$C_{44} = C_{55} = C_{66} = C_{44}^{o} - 2\lambda_3^2(R_{11} + R_{12})q_1^2$$

$$C_{46} = C_{45} = C_{56} = -\lambda_3^2(R_{11} + 3R_{12})q_1^2$$

$$C_{36} = C_{14} = C_{25} = -\lambda_3\left[R_{11}\left(4\lambda_1 - \frac{8}{\sqrt{3}}\lambda_2\right) + R_{12}\left(8\lambda_1 + \frac{8}{\sqrt{3}}\lambda_2\right)\right]q_1^2$$

$$C_{24} = C_{15} = C_{34} = C_{35} = C_{26} = C_{16} = -\lambda_3\left[R_{11}\left(4\lambda_1 + \frac{4}{\sqrt{3}}\lambda_2\right) + R_{12}\left(8\lambda_1 - \frac{4}{\sqrt{3}}\lambda_2\right)\right]q_1^2$$

$$R_{11} = \frac{m + n}{m^2 + mn - 2n^2} \qquad R_{12} = \frac{-n}{m^2 + mn - 2n^2}$$

$$m = \left(2b + 2b' + \frac{2\lambda_3^2}{C_{44}^{o}}\right)q_1^2 \qquad n = \left(2b - \frac{\lambda_3^2}{C_{44}^{o}}\right)q_1^2$$

Thomas ([1970](#)) showed that expressions for the individual moduli are given by

$$C_{ij} = C_{ij}^{o} \sum_{k,l} \frac{\partial^2 G}{\partial e_i \partial q_k} R_{kl} \frac{\partial^2 G}{\partial e_j \partial q_l}. \qquad (21)$$

The matrix R_{kl} is strictly the inverse of the matrix, $\partial^2 G/\partial q_l \partial q_m$, i.e.

$$\sum_l R_{kl} \frac{\partial^2 G}{\partial q_l \partial q_m} = \delta_{km}. \qquad (22)$$

($(\partial^2 G/\partial q_l \partial q_m)$ is referred to here and below as the susceptibility matrix). Double differentiation is of the full Landau expansion, equation ([1](#)), with the order parameter components and strains then set to their equilibrium values. For $Pm\bar{3}m \leftrightarrow R\bar{3}c$, the susceptibility matrix contains two distinct terms, m and n, where:

$$m = \frac{\partial^2 G}{\partial q_1^2} = \frac{\partial^2 G}{\partial q_2^2} = \frac{\partial^2 G}{\partial q_3^2} = \left(2b + 2b' + \frac{2\lambda_3^2}{C_{44}^{o}}\right)q_1^2 \quad (23)$$

$$n = \frac{\partial^2 G}{\partial q_1 \partial q_2} = \frac{\partial^2 G}{\partial q_1 \partial q_3} = \frac{\partial^2 G}{\partial q_2 \partial q_3} = \left(2b - \frac{\lambda_3^2}{C_{44}^{o}}\right)q_1^2. \quad (24)$$

In the inverse matrix, R_{kl}, the diagonal terms are

$$R_{11} = R_{22} = R_{33} = \frac{m + n}{m^2 + mn - 2n^2} \qquad (25)$$

and the off-diagonal terms are

$$R_{12} = R_{13} = R_{23} = \frac{-n}{m^2 + mn - 2n^2}. \qquad (26)$$

Expressions for the single crystal moduli obtained in this way, maintaining the reference system of the cubic parent structure, are listed in table [2](#).

Values for b and b' must be obtained separately if a quantitative analysis of the elastic modulus variations is required. An independent source of data relating to these coefficients comes from soft mode frequencies. The soft mode for the transition above T_c splits into two separate modes below T_c, which have A_{1g} and E_g symmetry and frequencies ω_A and ω_E. The squares of these frequencies are expected to be proportional to the eigenvalues of the susceptibility matrix. If the susceptibilities are derived from the renormalized Landau expansion, (equation ([11](#))) the ratio of the frequencies will be related simply to the values of the Landau coefficients according to (from Thomas and Müller [1968](#), Harley *et al* [1973](#))

$$\frac{3\omega_E^2}{\omega_A^2 + 2\omega_E^2} = \frac{B - C}{B} = \frac{b'^*}{b^* + b'^*}. \qquad (27)$$

A modified perspective on the soft mode behaviour is that the frequencies depend on the unrenormalized Landau expansion (Slonczewski and Thomas [1970](#), Ishidate and Isonuma [1992](#)). Eigenvalues of the $\partial^2 G/\partial q_l \partial q_m$ matrix for the $R\bar{3}c$ structure are $m - n$, $m - n$ and $m + 2n$, giving

$$\frac{\omega_E^2}{\omega_A^2} = \frac{m - n}{m + 2n} = \frac{2b' + 3\lambda_3^2/C_{44}^{o}}{6b + 2b'}. \qquad (28)$$

In the case of SrTiO$_3$, use of the unrenormalized expansion provides a close, though not exact, description of the soft mode frequency variations (Carpenter [2007](#)).

3. Calibration of Landau coefficients

The determination of order parameter evolution with the highest resolution is provided by the symmetry breaking strain, e_4, extracted from powder neutron diffraction data (Hayward *et al* [2005](#)), where

$$e_4 = \frac{a}{a_o} \cos\alpha. \qquad (29)$$

Here a and α are lattice parameters of the rhombohedral structure, while a_o is the equivalent cell dimension of the cubic structure extrapolated to below T_c. Values of e_4 from the data
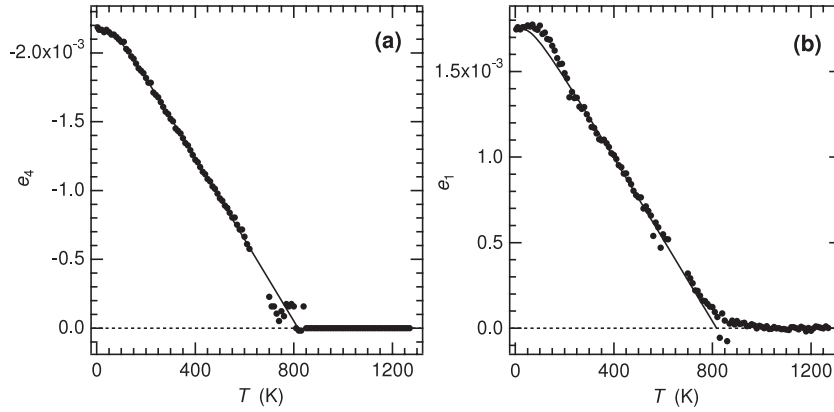
Figure 1. Temperature dependence of spontaneous strains from the high resolution powder neutron diffraction data for lattice parameters from Hayward *et al* (2005). (a) The solid line is a fit of equation (30) to the symmetry breaking strain, e_4, in the temperature interval 4.2–520 K with T_c fixed at 817 K. (b) The solid line is a fit of equation (30) to the non-symmetry breaking strain, e_1, in the temperature interval 270–520 K with fixed values of $\Theta_s = 95$ K and $T_c = 817$ K.

of Hayward *et al* (2005) are reproduced in figure 1(a) and have been used to obtain a fit to the expression

$$e_4(\propto q_1^2) \propto \left(\coth\left(\frac{\Theta_s}{T_c}\right) - \coth\left(\frac{\Theta_s}{T}\right) \right). \quad (30)$$

In order to exclude any of the possible contributions of non-linearities close to T_c discussed in detail by Hayward *et al* (2005), the fit was made only to data in the temperature interval 4.2–520 K, yielding $T_c = 814 \pm 3$ K, $\Theta_s = 97 \pm 3$ K, and $e_4 = -0.0022$ at 0 K. A value of $T_c = 817$ K has been preferred because it corresponds to the sharp maximum in heat capacity observed by Bueble *et al* (1998). Refitting the data with T_c fixed at 817 K gave $\Theta_s = 95$ K (the value also obtained by Hayward *et al* 2002) and, hence, $(q_1^2 + q_2^2 + q_3^2)_s = 0.884$ at 0 K, when $(q_1^2 + q_2^2 + q_3^2)_o = 1$. Figure 1(b) shows the variation of $e_1(=[a - a_o]/a_o)$ from the same original set of lattice parameters (Hayward *et al* 2005). The variation of a_o was determined by fitting the function $a_o = a_1 + a_2\Theta_{s,ao} \coth(\Theta_{s,ao}/T)$ (Salje *et al* 1991, Meyer *et al* 2000, 2001, Sondergeld *et al* 2000, Carpenter *et al* 2003) to data for the cubic lattice parameter in the temperature interval 1000–1270 K ($\Theta_{s,ao} = 181.4$, $a_1 = 7.5414$ Å, $a_2 = 0.0000937$ Å). Absolute values of e_1 are poorly constrained due to the uncertainty associated with extrapolating a_o below T_c, but a fit to data in the temperature interval 270–520 K, using the function on the right-hand side of equation (30) with Θ_s and T_c fixed at 95 and 817 K respectively, is shown. This gives $3e_1(=e_a) = 0.0052$ at 0 K.

Values of the bare elastic moduli, C_{11}^o, C_{12}^o and C_{44}^o have been taken as the values of the cubic phase at 817 K, obtained by linear extrapolation from high temperatures (figure 4 of Carpenter *et al* 2010a), i.e. 317, 131 and 157 GPa respectively. Equations (5) and (8) then yield $\lambda_1 = -1.14$, $\lambda_3 = 1.17$ GPa, using the values of q and e at 0 K given above. An alternative method of extracting a value for λ_1 is through the pressure dependence of the $Pm\bar{3}m \leftrightarrow R\bar{3}c$ transition. The relationship between transition pressure, P_c, and transition temperature, T_c,
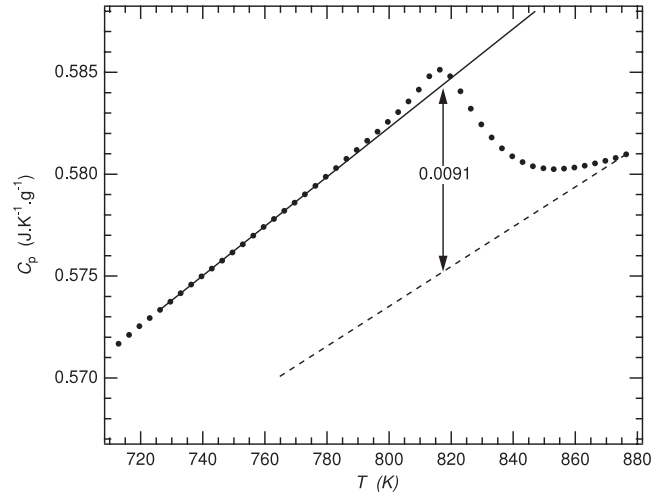

Figure 2. Heat capacity data of Hayward *et al* (2005) in the vicinity of the $Pm\bar{3}m \leftrightarrow R\bar{3}c$ transition. The broken line is the estimate of Hayward *et al* (2005) for the extrapolated heat capacity of cubic LaAlO$_3$. The estimated step in C_p at 817 K, 0.0091 J K^{-1} g^{-1}, excludes an additional small excess heat capacity in the data close to T_c. Note that the temperature interval for this small additional excess heat capacity coincides with anomalous variations in elastic properties reported below for ~797–817 K. The data are closely similar to those reported by Bueble *et al* (1998).

is given by (Carpenter 2007)

$$P_c = \frac{a\Theta_s \frac{1}{3} \left(C_{11}^o + 2C_{12}^o\right)}{2\lambda_1} \left(\coth\left(\frac{\Theta_s}{T}\right) - \coth\left(\frac{\Theta_s}{T_c}\right) \right). \quad (31)$$

Bouvier and Kreisel (2002) showed that the transition is second order in character, with $P_c = 13.8$ GPa at room temperature. For $T = 295$ K, values of Θ_s, T_c, C_{11}^o, C_{12}^o given above and $a = 0.000117$ GPa (below), this gives $\lambda_1 = -0.42$ GPa.

Values of the Landau coefficients a, b^* and b'^* have been obtained by combining heat capacity and Raman data from Hayward *et al* (2005). Figure 2 shows heat capacity data from figure 16 of Hayward *et al* (2005) and an estimate of the step in C_p, ΔC_p, at 817 K. The additional small anomaly evident
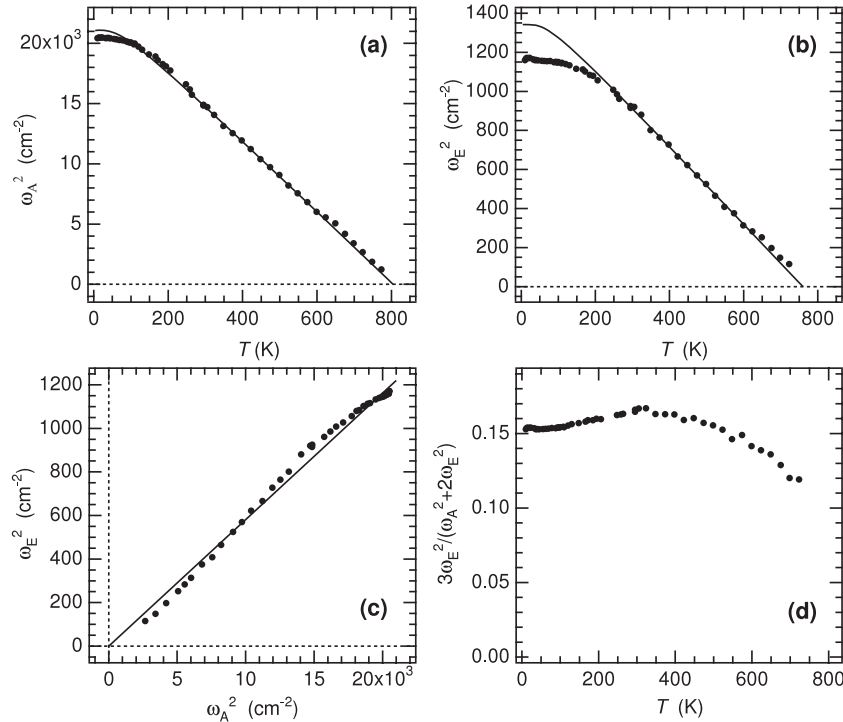
Figure 3. Soft mode frequency variations from Raman spectroscopic data of Hayward *et al* (2005). (a) The solid line is a fit to the expression on the right-hand side of equation (30), using data in the temperature interval ∼265–520 K with Θ_s fixed at 95 K. (b) The solid line is a fit to the data obtained in the same way as for (a). (c) The straight line was fit to data above room temperature and constrained to pass through the origin. It has a slope of 0.0581. (d) The combination of frequencies on the left axis was taken from equation (27) and is expected to be constant for a classical second order transition.

in the data close to T_c was excluded when estimating $\Delta C_p =$ 0.0091 J K^{-1} g^{-1} = 1.95 J mol^{-1} K^{-1}. Equation (19) then gives $a = 3.90$ J mol^{-1} K^{-1} and $3b^* + b'^* = 9558.9$ J mol^{-1}. In principle the soft mode frequencies for the rhombohedral phase give the ratio of b^* to b'^* or b to b' according to equations (27) or (28). Raman data for the A$_{1g}$ and E$_g$ soft modes given by Hayward *et al* (2005) are therefore reproduced here in figure 3 as plots of ω_A^2 versus T, ω_E^2 versus T, ω_E^2 versus ω_A^2 and $3\omega_E^2/(\omega_A^2 + 2\omega_E^2)$ versus T. Given that the soft mode frequencies are expected to scale as $\omega^2 \propto q^2$, fits to the data in figures 3(a) and (b) were obtained in the same way as the fit to e_4 in figure 1(a). Only data in the temperature interval ∼265–525 K were used for the fitting and the value of Θ_s was held fixed at 95 K. On this basis, ω_A^2 and ω_E^2 would extrapolate to zero at 805 ± 4 and 760 ± 7 K, respectively, if their linear trends were maintained. The straight line constrained to pass through the origin in figure 3(c) was fit to data collected above room temperature and corresponds to $\omega_E^2/\omega_A^2 = 0.0581$. If it is assumed that the soft mode frequencies depend on the unrenormalized susceptibilities (equations (23) and (24)), this slope gives a value of the right-hand side of equation (28) which can be combined with the $3b^* + b'^*$ value from ΔC_p to determine values for b and b'. On the other hand, if the soft mode frequencies follow the renormalized susceptibilities, the ΔC_p result can be combined with the ratio of frequencies expressed in equation (27). It turns out that the former give degrees of elastic softening for C_{44} at room temperature which are larger than observed, while the latter leads to a calculated value of C_{44} which is consistent with the observed softening

(see below). The Landau parameters listed in table 3 as best fit parameters are therefore for the renormalized case using the room temperature value of $3\omega_E^2/(\omega_A^2 + 2\omega_E^2) =$ 0.167. Adjustments were made to the values of λ_1 and λ_2 by iteration so that calculated softening of the bulk modulus, K, and $\frac{1}{2}(C_{11} - C_{12})$ matched with observed values at room temperature from Carpenter *et al* (2010a). Conversion of units from J mol^{-1} to GPa (1 J mol^{-1} = 3.002 × 10^{-5} GPa) has been achieved by assuming a constant molar volume for LaAlO$_3$ of 33.31×10^{-6} m^3, corresponding to that of the cubic form at ∼820 K.

4. Experimental methods

The two single crystal plates of LaAlO$_3$ used for Brillouin spectroscopy *in situ* at high temperatures were the same as described by Carpenter *et al* (2010b) for room temperature measurements. These had been polished parallel to (110) and (100), respectively, and were 190 ± 1 μm thick. The (110) plate had dimensions of ∼0.5 × 1.0 mm, and contained a central portion from which Brillouin spectra could be collected that was free of optically visible twins. It may have contained twins with $\bar{3}$ axes parallel to [111] and [$\bar{1}\bar{1}1$], respectively, coexisting across (110) twin planes. However, as discussed by Carpenter *et al* (2010b), these would give acoustic phonon velocities in the (110) plane which are for the same crystallographic directions. The (100) plate had dimensions of ∼1 × 1 mm and contained multiple lamellar twins. Brillouin spectra collected from this plate at room temperature were interpreted

Table 3. Values of Landau parameters extracted from experimental data for the spontaneous strain e_4, ΔC_p at 817 K and soft mode frequencies, together with observed values of bulk modulus and $\frac{1}{2}(C_{11} - C_{12})$ at room temperature. The Landau model is for a second order transition with soft mode frequencies determined by renormalized order parameter susceptibilities.

$a = 0.000\,117$ GPa K^{-1}	3.90 J mol^{-1} K^{-1}
$b^* = 0.089\,66$ GPa	2986.7 J mol^{-1}
$b'^* = 0.017\,98$ GPa	598.9 J mol^{-1}
$b = 0.097\,58$ GPa	3250.4 J mol^{-1}
$b' = 0.022\,47$ GPa	748.5 J mol^{-1}
$\Theta_s = 95$ K	
$T_c = 817$ K	
$\lambda_1 = -0.59$ GPa	
$\lambda_2 = -0.32$ GPa	
$\lambda_3 = 1.17$ GPa	
$C_{11}^o = 317$ GPa	
$C_{12}^o = 131$ GPa	
$C_{44}^o = 157$ GPa	
$(K^o = \frac{1}{3}(C_{11}^o + 2C_{12}^o) = 193$ GPa$)$	
$(R_{11} = 9.906$ GPa, $R_{12} = -4.160$ GPa$)$	

Table 4. Single crystal elastic moduli, with respect to cubic reference axes, obtained by fitting to Brillouin velocity data collected from the (110) plate. Values of the bulk and shear moduli are Voigt–Reuss–Hill averages determined from the single crystal data.

T (K)	C_{11} (GPa)	C_{12} (GPa)	C_{44} (GPa)	C_{46} (GPa)	C_{36} (GPa)	C_{24} (GPa)	K_H (GPa)	G_H (GPa)
293[a]	286.5	150.0	149.0	3.9	−25.0	15.0	195.5	105.3
293	283.4	148.3	149.3	3.6	−26.9	13.6	193.4	104.9
373	282.4	146.7	148.5	2.8	−26.5	13.4	191.9	104.9
473	280.7	144.8	146.1	2.9	−26.2	12.6	190.1	104.1
573	276.2	144.6	143.2	2.8	−25.3	13.1	188.5	101.4
673	268.6	145.7	140.3	5.6	−23.9	13.6	186.6	97.2
723	262.8	147.5	136.0	6.8	−23.2	14.5	185.9	92.5
748	258.0	147.0	132.2	7.6	−24.6	14.1	184.0	89.1
773	249.9	149.6	128.2	10.4	−22.4	14.6	183.0	83.7
793	246.7	148.9	109.7	16.6	−28.9	6.5	182.0	74.2
808[b]	248.8	94.7	93.5	24.0	−36.2	−50.3	124.0	81.4
818	309.3	129.7	152.7	0	0	0	189.5	123.4
843	313.7	129.4	156.3	0	0	0	190.8	126.5
923	312.2	129.2	154.6	0	0	0	190.2	125.3
1000	307.4	128.6	154.8	0	0	0	188.2	124.2

[a] Best fit data set of Carpenter *et al* (2010b), determined by fitting to velocities from (110) and (100) plates simultaneously.
[b] Fitted parameters for 808 K should be treated with scepticism since they are based on velocities estimated from broad Brillouin peaks and include data for only one TA-wave peak.

as including contributions from two separate twin orientations (Carpenter *et al* 2010b). As also described in detail by Carpenter *et al* (2010b), the plates were held within 350 μm thick pieces of Pt foil from which holes had been cut to match their shapes. The (110) plate was held in place during loading into the furnace by a small quantity of 'Resbond 940' ceramic cement placed at both ends and cured for 10 min at ∼373 K. It is likely that this cracked during the first heating runs so that it did not provide a source of stress on the crystal. The (100) plate sat freely within the space cut through the Pt foil.

In the furnace used for *in situ* data collection at high temperatures (Sinogeikin *et al* 2000, Jackson *et al* 2000, Schilling *et al* 2003b, 2003a), the sample is located at the centre of a circular resistance heater, with glass windows at each end to permit access of the laser beam. During heating runs, temperature was measured using a K-type (chromel–alumel) thermocouple which rested against the Pt foil, close to the sample (see figure 5 of Sinogeikin *et al* 2000). Temperature stability during collection of each data set was within ∼0.5 °C. As the hot zone of the furnace was enclosed by glass windows, any temperature gradients across the sample should have been small. Previous high temperature experiments in this furnace reproduced the transition point at 573 °C in quartz to within 2–3 °C, so uncertainties in absolute values of measured temperatures in the present study are expected to be of the same order.

The Brillouin spectrometer used for data collection has also been described elsewhere (e.g. Schilling *et al* 2003a, Palko *et al* 2002). The light source, focusing, optical geometry, polarization and Brillouin shift/phonon velocity relationships were the same as used by Carpenter *et al* (2010b). Measurements of spectra spaced at 15° intervals round the chi circle (the plane of the single crystal plate) at room temperature were used to determine prominent symmetry axes,

including [001] and [$\bar{1}$10] within the (110) plate or [010], [001], [011] and [0$\bar{1}$1] within the (100) plate. High temperature spectra were collected both round the chi circle at fixed temperatures and through a succession of temperatures with fixed orientations. For changes in temperature of only a few degrees, a thermal equilibration time of ∼5 min was allowed. For larger temperature intervals, the equilibration time was ∼20 min. Each spectrum was an accumulation of ∼180–1600 frequency scans of ∼0.5 s (0.5 ms per channel, 1024 channels). For direct comparison between spectra, intensities have been rescaled to the equivalent of 500 scans per spectrum. In order to relate changes in the Brillouin spectra to any changes in twin configuration, images of the crystals *in situ* at high temperatures were recorded using an optical microscope setup with a video camera.

Observed acoustic phonon velocities for general directions were converted to elastic moduli, C, as $C = \rho V^2$, where the density, ρ, was taken to be 6.52 g cm^{-3} at room temperature. Density variations at high temperatures were calculated using the lattice parameter data of Hayward *et al* (2005). As described in Carpenter *et al* (2010b), complete sets of moduli at room temperature were obtained by fitting to observed velocity variations and using the reference axes for a trigonal crystal in which (110)$_{\text{cubic}}$ becomes $(0\sqrt{2}1)_{\text{trigonal}}$ and (100)$_{\text{cubic}}$ becomes $(\sqrt{3}\bar{1}\sqrt{2})_{\text{trigonal}}$. The 'best fit' values of moduli at room temperature were obtained by fitting to velocities round the chi circles for both plates simultaneously for a single twin orientation which had [111] as the $\bar{3}$ axis (twin I in figures 1 and 2 of Carpenter *et al* 2010b). At high temperatures in the stability field of the $R\bar{3}c$ phase, data from only the (110) plate were used for the fitting. Using this smaller number of data points gives slightly different values for the moduli in comparison with values obtained by fitting to the complete (110) and (100) velocities together (see table 4). Data collected
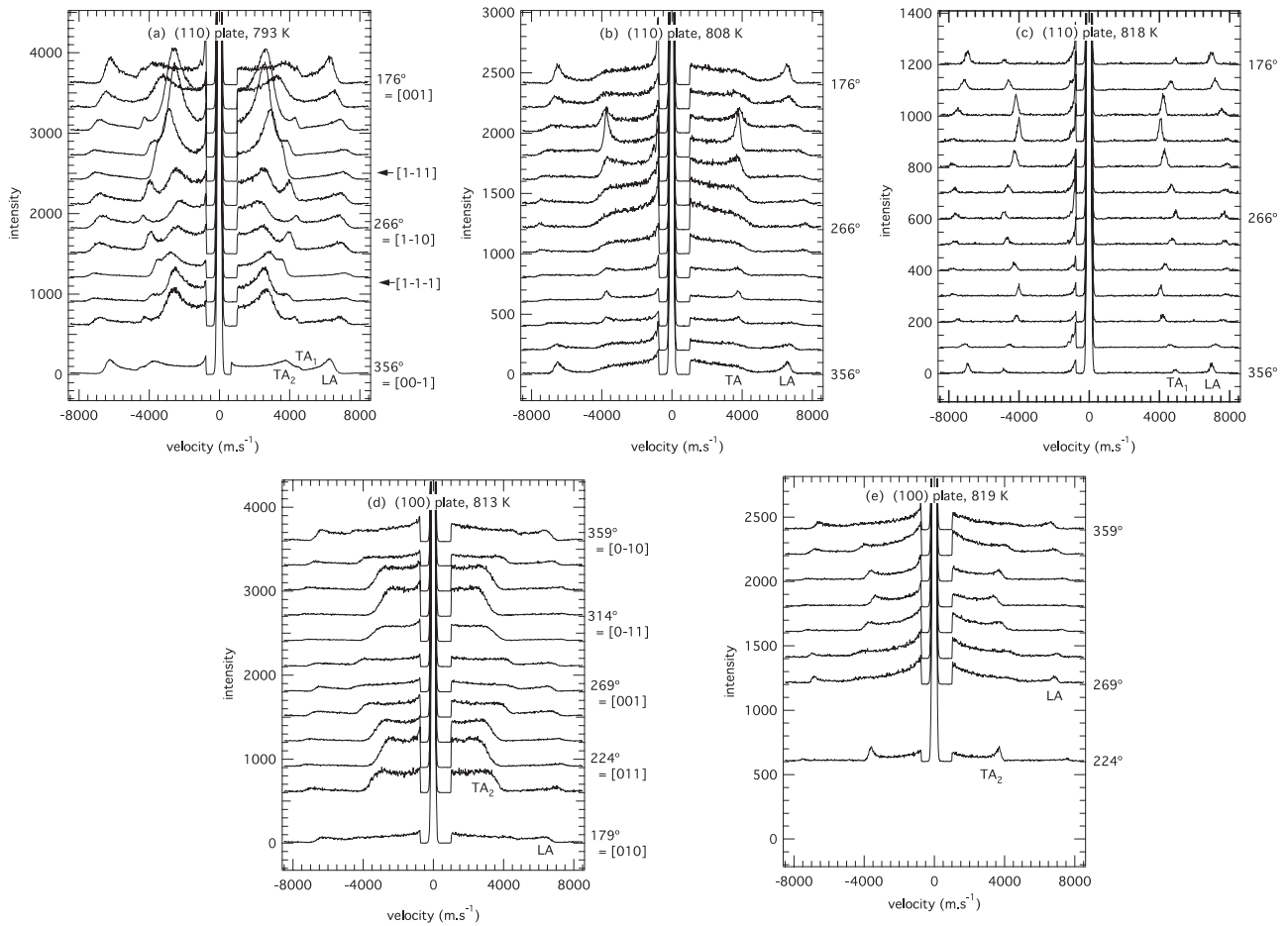
Figure 4. Brillouin spectra collected around the chi circle for (110) and (100) plates at temperatures close to the $Pm\bar{3}m \leftrightarrow R\bar{3}c$ transition point. Chi angles for selected crystallographic directions are indicated in degrees. Labels LA, TA$_1$ and TA$_2$ correspond to the elastic modulus combinations listed in table 3 of Carpenter *et al* (2010b) (a) (110) plate, 793 K. LA, TA$_1$ and TA$_2$ peaks are all visible but are substantially broader than at room temperature. (b) (110) plate, 808 K. Only one TA-wave peak is visible and spectra are dominated by the central peak. (c) (110) plate, 818 K. Spectra have narrow LA- and TA-wave peaks, characteristic of the $Pm\bar{3}m$ phase. (d) (100) plate at 813 K. Spectra are dominated by the central peak and only one TA-wave peak can be distinguished. (e) (100) plate at 819 K. Spectra are similar to those in (d) but LA- and TA-wave peaks are more clearly defined and the intensity of the central peak is diminished.

above the $Pm\bar{3}m \leftrightarrow R\bar{3}c$ transition temperature were fit using cubic reference axes.

5. Results

5.1. High temperature data for variable crystallographic directions within single crystal plates

Spectra for seven directions around the chi circle of the (110) plate were collected at 373, 473, 573, 673 K, and for 13 directions around the chi circle at 723, 748, 773, 793, 808, 818, 848, 923 and 1000 K. Apart from small shifts in peak velocities, spectra collected at temperatures up to 723 K were closely similar to spectra collected at room temperature. Starting at ∼725 K, however, individual peaks became progressively broader, and a broad central peak with increasing intensity developed, as illustrated for 793 K in figure 4(a). At 808 K, the spectra became dominated by the central peak (figure 4(b)) but at 818 K they had reverted to standard spectra with relatively sharp peaks and a flat background (figure 4(c)). Elastic moduli from fits to the

velocity variations in chi circle data sets up to 793 K are listed in table 4. The fitting was completed for the trigonal reference system and converted to cubic reference axes using the expressions listed in table 1 of Carpenter *et al* (2010b). Spectra collected round the chi circle of the (100) plate at 813 K were also dominated by the broad central peak (figure 4(d)). Sharper peaks are present in spectra collected at 819 K (figure 4(e)).

Spectra collected from the (110) plate at 818, 843, 923 and 1000 K, and from the (100) plate at 1000 K each contained one LA-wave peak and one TA-wave peak, consistent with point group symmetry *m3m*. Separate fits to 1000 K data for the (110) and (100) plates gave $C_{11} = 307.4 \pm 1.5$, $C_{12} = 128.6 \pm 1.5$, $C_{44} = 154.8 \pm 0.8$ and $C_{11} = 309.1 \pm 0.6$, $C_{12} = 129.5 \pm 0.8$, $C_{44} = 153.1 \pm 0.5$ GPa, respectively (for $\rho = 6.385$ g cm^{-3}). Observed velocities and velocities calculated from the average of these two fits ($C_{11} = 308.3$, $C_{12} = 129.1$, $C_{44} = 154.0$ GPa) are compared directly in figure 5. These data and cubic fits for the (110) plate at 818, 843, 923 K are also listed in table 4. All the fitted moduli, defined with respect to the cubic reference system, are plotted
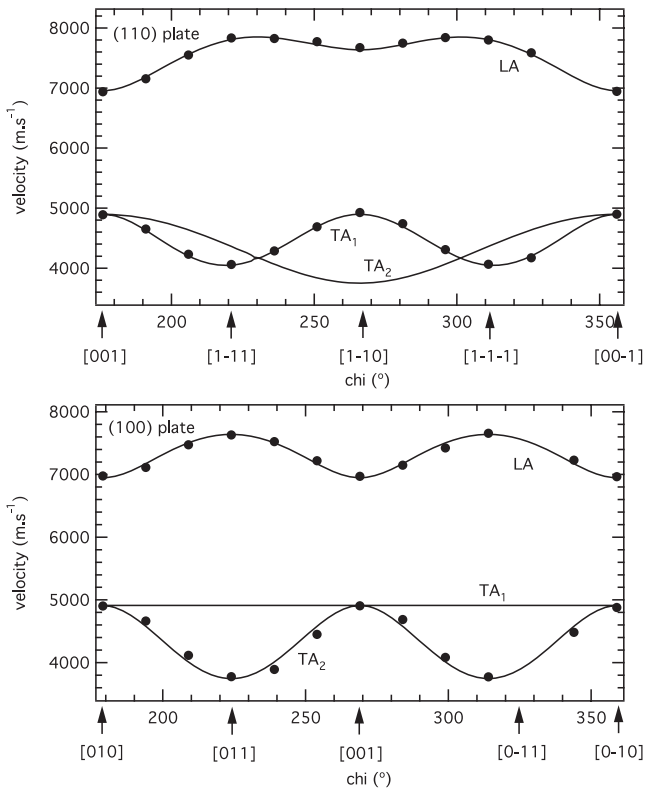
Figure 5. Phonon velocities as a function of chi angle for directions within the (110) and (100) plates at 1000 K. Solid lines are calculated variations based on the average values from separate fits to data for the (100) and (110) plates ($C_{11} = 308.3$, $C_{12} = 129.1$, $C_{44} = 154.0$ GPa, for $\rho = 6.385$ g cm^{-3} at 1000 K).

Figure 6. Observed and calculated elastic moduli through the $Pm\bar{3}m \leftrightarrow R\bar{3}c$ transition of LaAlO$_3$. Top: single crystal data. Bottom: average of Voigt and Reuss limits for bulk and shear moduli calculated from the single crystal data. Open symbols are observed values from RUS, filled symbols are Brillouin values. Crosses are 'best fit' values obtained by simultaneous fitting to data from (110) and (100) plates collected at room temperature (Carpenter *et al* 2010b) or by averaging separate fits to data from the (100) and (110) plates collected at 1000 K. Values of elastic moduli for 808 K should be treated with scepticism. Broken lines are fits to RUS data for the cubic phase in the temperature range 885–1036 K:
$C_{11}^{\rm o} = 353.84 - 0.045\,386T$, $C_{12}^{\rm o} = 134.61 - 0.004\,962T$,
$C_{44}^{\rm o} = 169.82 - 0.016\,081T$, with $K^{\rm o} = 207.65 - 0.018\,389T$ and
$\frac{1}{2}(C_{11}^{\rm o} - C_{12}^{\rm o}) = 109.61 - 0.020\,212T$ obtained by combining these fit parameters. $G^{\rm o} = 142.66 - 0.018\,965T$ is a fit to the data for G from the same temperature interval. Solid lines are calculated variations for the $R\bar{3}c$ phase obtained using the expressions in table 2 and the parameters listed in table 3.

as a function of temperature in figure 6. Given the broadness of peaks in spectra collected at 808 K, the elastic modulus values given in table 4 for this temperature should be treated with scepticism.

5.2. High temperature data for selected crystallographic directions

Several heating sequences were followed with the plates held at fixed orientations so as to collect velocity data for specific crystallographic directions at small temperature intervals through the $Pm\bar{3}m \leftrightarrow R\bar{3}c$ transition. For the (110) plate, chi $= 266°$ and $356°$ ($+$ the equivalent $176°$), corresponding to $[1\bar{1}0]$ and $[00\bar{1}]$ ($+$ the equivalent $[001]$) directions, were chosen. In the case of chi $= 266°$, spectra were collected during two separate heating sequences and included three spectra collected at 823, 808 and then 788 K during subsequent cooling from 1036 K. In the case of chi $= 176°$, spectra were collected during both heating and cooling between 793 and 818 K. For the (100) plate, the chosen directions were at chi $= 224°$ and $359°$, corresponding to [011] and [0$\bar{1}$0]. Velocities from LA- and TA-wave peaks were converted to elastic moduli using densities corrected for thermal expansion, as described above, and the full sets of data are displayed in figure 7. Labels LA, TA$_1$ and TA$_2$ have been added to correspond with elastic combinations which determine the acoustic phonon velocities as listed in table 3 of Carpenter *et al* (2010b). It should be noted that velocity
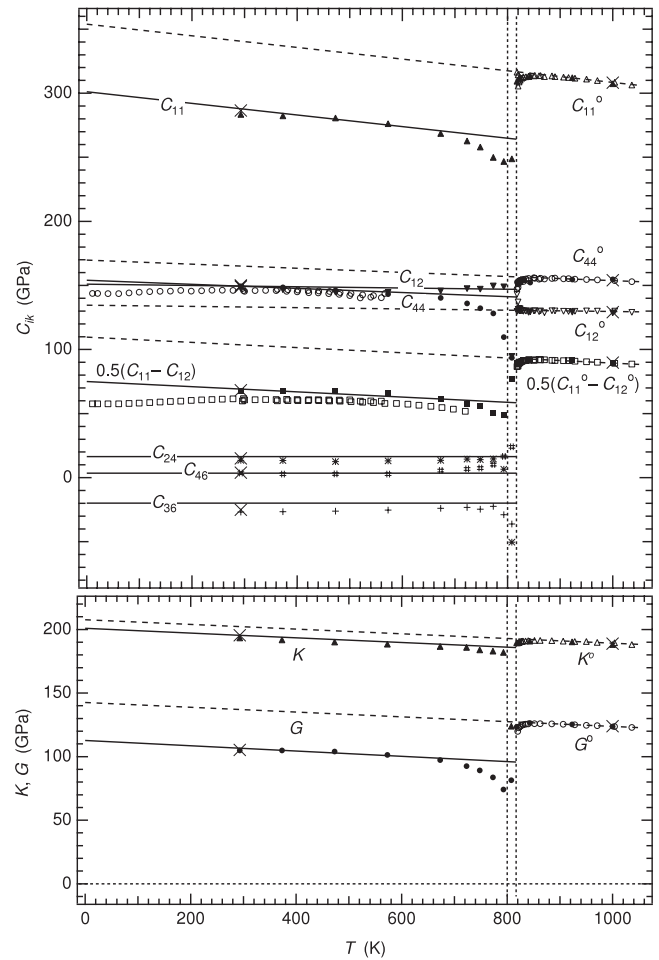
data from the (100) plate show higher symmetry than is permitted under point group $\bar{3}m$ symmetry (Carpenter *et al* 2010b). Additional peaks observed in the room temperature spectra indicated that at least two twin components were being sampled by the laser beam. TA$_1$-waves for the [011] and [0$\bar{1}$1] directions are interpreted as having sufficiently similar velocities that their peaks overlap, as do the TA$_2$ peaks. This means that twins with [011] parallel to a diad are only distinguishable from twins in which [011] lies within a mirror plane by their LA-wave peaks (figure 2 and table 3 of Carpenter
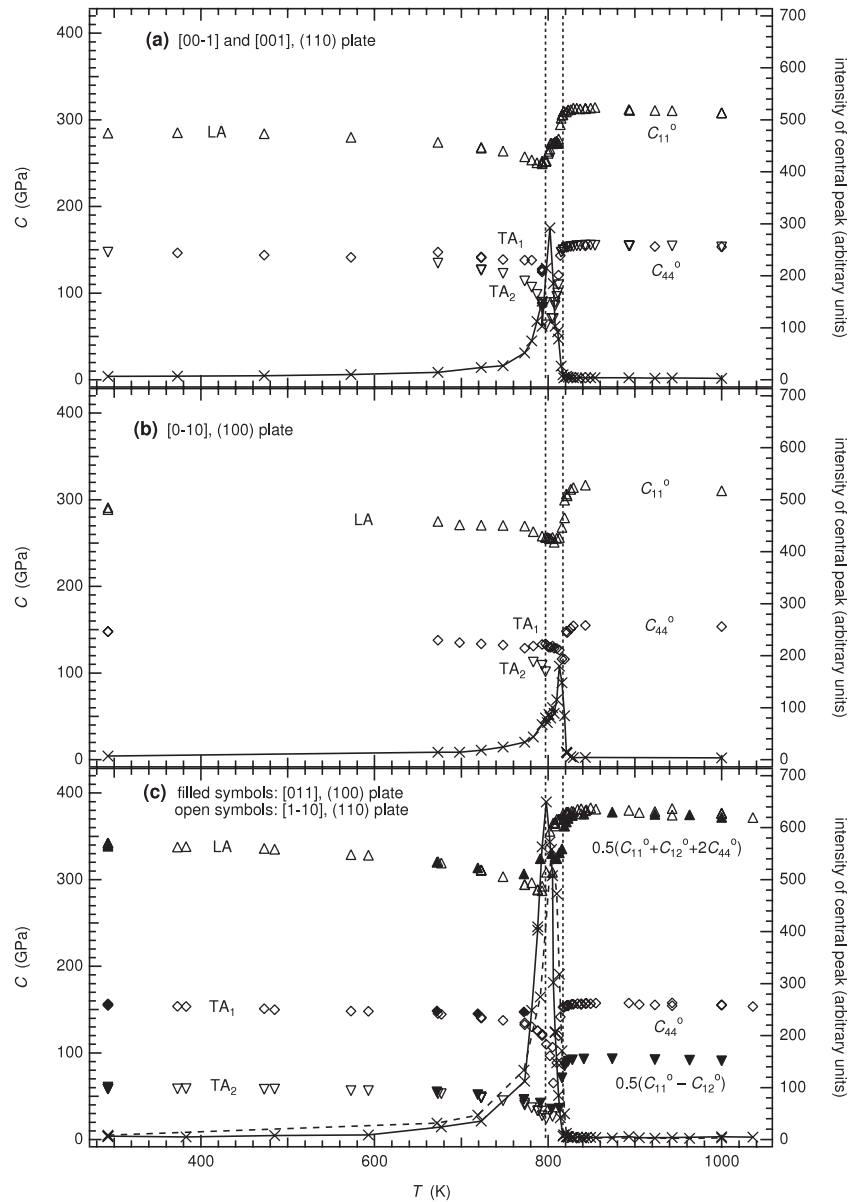
Figure 7. Elastic moduli for LA- and TA-waves obtained from Brillouin spectra collected for specific crystallographic directions (individual symbols, left axis). Labels LA, TA$_1$ and TA$_2$ correspond to the LA- and TA-waves listed in table 3 of Carpenter *et al* (2010b). Also shown are intensities of the central peak from the same spectra (crosses joined by lines, right axis), as measured close to the shutter which blocks the central beam from reaching the spectrometer. Vertical dotted lines are placed at 797 and 817 K. (a) TA$_1$ and TA$_2$ peaks in the [001] direction ((110) plate) overlap at room temperature but can be resolved above ∼650 K. The intensity of the central peak reaches a maximum at ∼800 K. (b) The pattern of elastic modulus variations for [0$\bar{1}$0] in the (100) plate is similar to that for [001] in the (110) plate except for within the temperature interval 797–817 K. The central peak intensity reaches a maximum at ∼813 K. (c) Elastic moduli for the [011] ((100) plate) and [1$\bar{1}$0] ((110) plate) directions show similar variations even though they are not related by symmetry in the stability field of the $\bar{3}m$ structure. This is interpreted as being due to the presence of peaks from two twin orientations in the (100) plate. Both sets of data are understood as being for directions parallel to a diad rather than within a mirror plane. Spectra from both plates have a maximum in the intensity of the central peak close to 800 K.

et al 2010b). The LA-wave for [0$\bar{1}$1] parallel to the diad gives a strong peak while the peak from the LA-wave for [011] within the mirror plane is weak. Thus the spectra are dominated by peaks from LA-waves travelling parallel to the diad in both the twin orientations sampled. The data in figure 7(c) are from strong peaks only and refer to LA-waves travelling parallel to [1$\bar{1}$0] and symmetry related directions in the $\bar{3}m$ structure.

With increasing temperature from room temperature in the $R\bar{3}c$ stability field, most of the elastic modulus trends

show a progressive softening which becomes most evident in the range ∼650–800 K. For the [001] ((110) plate) and [0$\bar{1}$0] ((100) plate) directions, the single shear wave peak at room temperature consists of two overlapping peaks, TA$_1$ and TA$_2$. These become two clearly resolved peaks at 673 K and above, with TA$_2$ showing a higher degree of softening than TA$_1$ as $T \to$ ∼800 K (figures 7(a) and (b)). Between ∼797 and ∼817 K, there is a more complex pattern of evolution, as shown in the expanded view given in figure 8. All the
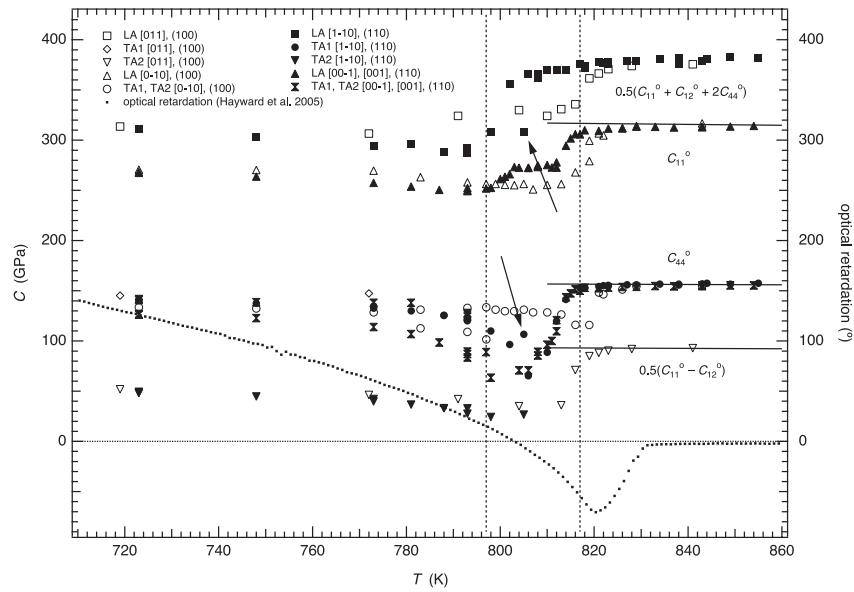
Figure 8. Expanded view of the elastic modulus data from figure 7 for temperatures in the vicinity of the $Pm\bar{3}m \leftrightarrow R\bar{3}c$ transition. Note that data from the 805 K spectrum (arrowed, [1$\bar{1}$0], (110) plate) fall off trend, but otherwise data collected during heating and cooling sequences define internally consistent patterns of variation with temperature. Optical retardation data from Hayward *et al* (2005) for a (110) plate have been added for comparison (dots, right axis). The crossover from positive to negative retardation corresponds more or less with the lower temperature limit of the anomalous elastic behaviour and the absolute minimum corresponds more or less with the transition temperature. Solid lines are fits to RUS data for the cubic phase taken from figure 6.

data show a discontinuity or break in trend at temperatures between ~812 and ~819 K, apart from those for the LA-wave travelling parallel to [1$\bar{1}$0] in the (110) plate. There is a clear discontinuity at ~817 K for the TA_1-wave travelling parallel to [0$\bar{1}$0] ((100) plate). The LA-wave for the [1$\bar{1}$0] ((110) plate) direction shows a break at ~800 K, which coincides with the additional break observed for the [001] direction in the (110) plate. Elastic moduli for TA_1-waves in the [1$\bar{1}$0] and [001] directions of the (110) plate appear to reduce to a minimum at ~807 K, though these values are subject to relatively large uncertainties due to the broadness of the TA-wave peaks in the original Brillouin spectra. Overall, elastic properties in the ~797–817 K interval are distinct from those of both the $R\bar{3}c$ and $Pm\bar{3}m$ phases.

In the stability field of the cubic phase, the moduli obtained from Brillouin measurements are essentially indistinguishable from those obtained by RUS (Carpenter *et al* 2010a) (figures 7 and 8). Both sets of data show a slight degree of softening for C_{11}, C_{44} and $\frac{1}{2}(C_{11} - C_{12})$ as T_c is approached from above.

5.3. Characterization of the central peak

Elastic softening in the $R\bar{3}c$ field is accompanied by large changes in the central peak of the Brillouin spectra. To illustrate this evolution, spectra collected through the transition for chi = 266° of the (110) plate, corresponding to the [1$\bar{1}$0] direction, and chi = 224° of the (100) plate, corresponding to the [011] direction, are shown in figures 9(a) and (b), respectively. Between ~800 and ~817 K the central peak becomes the dominant feature of each spectrum and the velocities of individual shear waves are hard to define. A

measure of the intensities of the central peak has been taken as the peak height in a small velocity range close to the region cut off from the detector. Variations of these intensities have been added to figure 7(c) and show a sharp maximum in the vicinity of 800 K, followed by a steep decline and return to baseline values at 817 K for the (110) plate and 821 K for the (100) plate. Above these temperatures the central peak effectively disappeared. Equivalent stacks of spectra for chi = 176° in the (110) plate (= [001]) and chi = 359° in the (100) plate (= [0$\bar{1}$0]) are shown in figures 9(c) and (d). Splitting of the TA_1 and TA_2 peaks and the rise in intensity of the central peak are visible in these. For the [001] direction, the central peak reached a maximum in intensity at ~800 K (figure 7(a)) but, for [0$\bar{1}$0], the maximum is at ~813 K (figure 7(b)). The central peak effectively disappeared at ~817 K and ~821 K, respectively. Uncertainty in temperature reproducibility between runs has been estimated to be 2–3 K. The difference between peak intensity temperatures of 800 and 813 is therefore significant, while the difference between 817 and 821 K might not be.

5.4. Characteristics of the 797–817 K interval

The complex pattern of elastic modulus variations in the 20 K interval between ~797 and 817 K, together with the evolution of central peaks with maxima at two different temperatures was an entirely unexpected feature of the $Pm\bar{3}m \leftrightarrow R\bar{3}c$ transition. Heating and cooling sequences through this interval for the [001] direction in the (110) plate (chi = 176°) gave quite reproducible spectra and peak velocities. One spectrum, collected at 805 K during the first heating of the (110) plate, did not follow this reversible trend, however (see
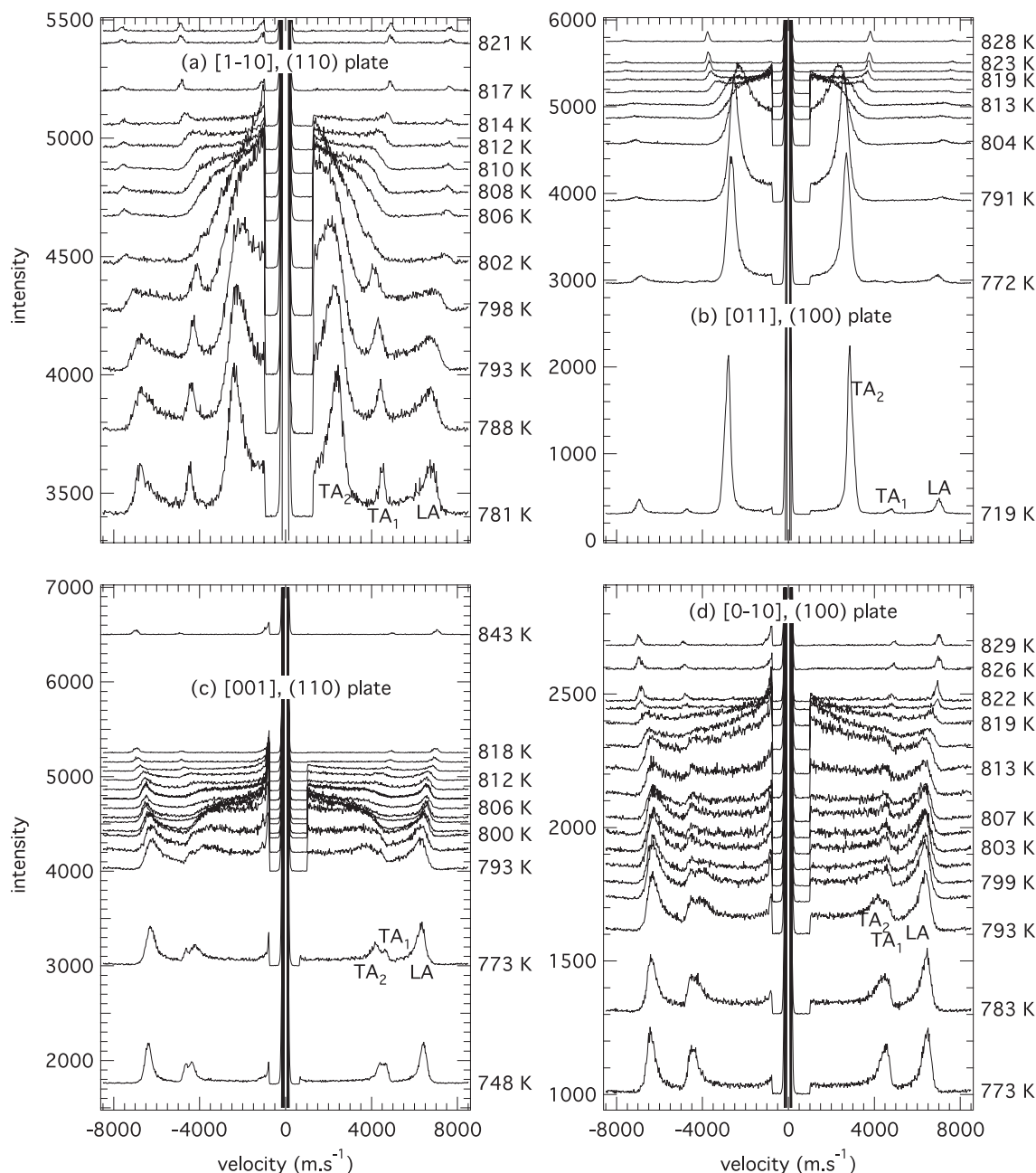
Figure 9. Brillouin spectra collected during heating and cooling sequences through the transition temperature for four different crystallographic directions. In each case, the spectra have been shifted up the *y*-axis in proportion to the temperatures at which they were collected. (a) [1$\bar{1}$0], (110) plate. (b) [011] direction, (100) plate. (c) [001] direction, (100) plate. (d) [0$\bar{1}$0] direction, (100) plate. Labels LA, TA$_1$ and TA$_2$ correspond to the LA- and TA-waves listed in table 3 of Carpenter *et al* (2010b).

data points indicated by arrows in figure 8). Either an incorrect temperature was recorded for this spectrum or there is some hysteresis in the change in spectral characteristics observed at ∼800 K. This is the only spectrum which did not conform to the detailed pattern of the intermediate temperature interval described here.

Spectra from (110) and (100) plates of the cubic form of LaAlO$_3$ contain one LA-wave peak and one TA-wave peak, consistent with the presence of {100} and {110} mirror planes in crystal class *m*3*m* (figures 4(c) and 9). Spectra from individual twins of the rhombohedral form contain one LA-

wave and two TA-wave peaks, consistent with $\bar{3}$*m* symmetry (figures 4(a) and 9). Spectra collected at 813 K from the (100) plate contain one LA-wave peak and one TA-wave peak (figure 4(d)), with velocity distributions (bearing in mind the uncertainty in defining peak positions for broad peaks) that have the same variation round the chi circle as shown by spectra from the cubic phase (figure 10(a)). At 808 K, the (110) plate also gave spectra containing only two peaks (figure 4(b)). In this case, the pattern of velocity variations round the chi circle differs substantially from the patterns shown by spectra from both the cubic and rhombohedral phases (figure 10(b)).

Systematic variations of peak widths round the chi circle are also evident in figures 4(b) and (d). TA-wave peaks are all broad, apart from for directions close to $[1\bar{1}1]$ and $[1\bar{1}\bar{1}]$ ((110) plate), where they are relatively narrow (figure 4(b)). LA-wave peaks are generally broad, but possibly at their broadest close to the $[1\bar{1}1]$ and $[1\bar{1}\bar{1}]$ directions where the TA-wave peaks are at their narrowest.

From the description above of modulus variations between ∼797 and ∼817 K, it appears that there is a 20 K interval below T_c in which the elastic behaviour of LaAlO$_3$ is distinctly different from that found in the rest of the $R\bar{3}c$ stability field. The observation of only one TA-wave peak, as for the $Pm\bar{3}m$ structure, implies that the symmetry on an acoustic phonon length scale is approaching cubic. Some of the moduli show obvious breaks at ∼802 and ∼813–819 K (figure 8), corresponding in some cases with the temperatures at which maxima in the intensities of the central peak also occur (figure 7). Velocities for the [001] ((110) plate) and $[0\bar{1}0]$ ((100) plate) directions should be identical for both $\bar{3}m$ and $m\bar{3}m$ symmetry, however, raising the possibility that there is an intermediate structure with different symmetry. In this context, the pattern of both LA- and TA-wave velocities in the (110) plate is also quite distinct (figure 10(b)). If LaAlO$_3$ adopts a different intermediate structure, its limits would be defined approximately by the maxima of the central peak intensities for the $[0\bar{1}0]$ and [001] directions. The attempted fit to chi circle data collected at 808 K gives elastic moduli which are significantly out of line from results for lower temperatures (table 4, figure 6), but cannot be given much credence in view of the uncertainty in defining the positions of broad peaks. Additional data in other crystallographic directions from those already collected would be needed to explore the full modulus matrix of a possible intermediate structure.

5.5. Evolution of microstructure

Video camera images of the (110) and (100) plates observed between crossed polars were examined during both heating and cooling cycles in an attempt to characterize any changes in microstructure through the 797–817 K interval. Figure 11 contains a representative selection of optical micrographs showing the (110) plate between crossed polars at different temperatures. The extinction position of the central portion of the crystal was always with its long axis vertical or horizontal (E–W and N–S polars). At temperatures of 820 K and above, the entire crystal was isotropic. It appeared to still be isotropic at 818 K (figure 11) but weak birefringence was clearly visible at 816 K, and this increased with falling temperature. Rotation of the crystal revealed a pattern of birefringence which appears to be related to strains arising at the edges of the crystal in the temperature range ∼797–817 K (e.g., see micrographs collected at 808 and 799 K). Below about 795 K, the birefringent edges of the crystal clearly contained traces of twin walls parallel to its length (e.g., 794 K micrograph). These edge regions then had a more uniform birefringence, with their extinction positions at an angle of ∼57° from the extinction position of the central portion. The width of the central portion decreased at lower temperatures, which can be understood in
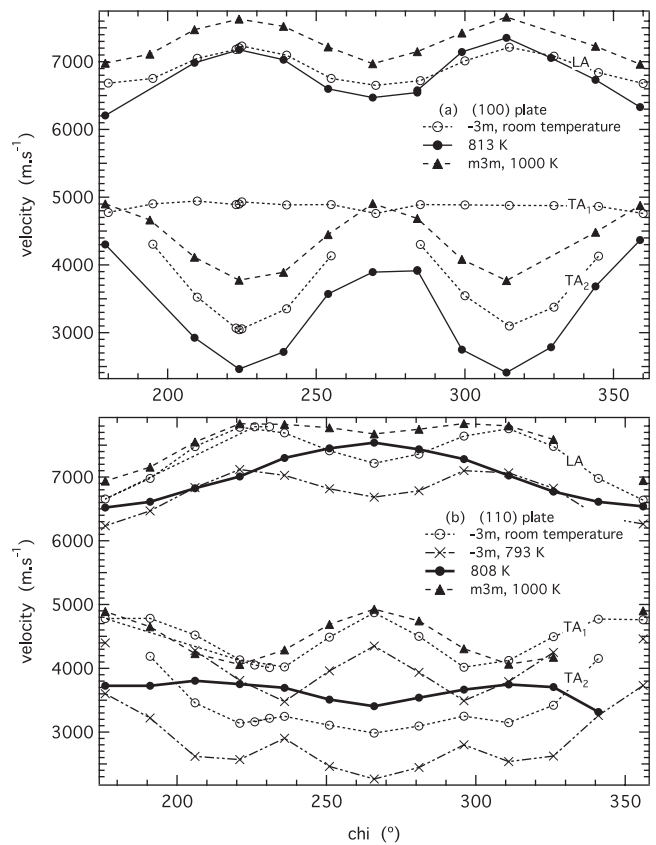

Figure 10. Velocities extracted from Brillouin spectra collected around the chi circle at temperatures within the $R\bar{3}c$ stability field, within the $Pm\bar{3}m$ stability and within the interval 797–817 K. (a) (100) plate. Only one TA-wave peak is observed at 810 K and this has the same pattern of velocity variation with chi angle as shown by the TA-wave of the cubic phase at 1000 K. (b) (110) plate. Only one TA-wave peak is seen at 808 K, but the pattern of velocity variations from both this peak and the LA-wave peak are quite different from patterns observed in the $R\bar{3}c$ or $Pm\bar{3}m$ stability fields.

terms of a change in the volume fraction of different twins. The birefringence of the whole crystal also increased. This sequence of isotropic character down to ∼817 K, uniform birefringence between ∼817 and ∼797 K apart from local strain effects, and the presence of distinct macroscopic twin orientations below ∼797 K was reproducible in both heating and cooling sequences.

Figure 12 contains a representative selection of optical micrographs showing the (100) plate between crossed polars at different temperatures. The plate appeared to be essentially isotropic at 822 K. A faint development of birefringence was apparent with the crystal held in the 45° position at 821 K, and this became more evident at 820 K (figure 12). By 817 K, there was a distinct tweed-like texture of diffuse cross-hatched twins with traces lined up parallel to (010) and (001); this is illustrated in the optical micrograph obtained at 816 K. At lower temperatures the microstructure seemed only to become better defined, with a relatively small amount of domain coarsening. There was no obvious change near ∼800 K, though at temperatures between 804 and 817 K, at least, an unusual pattern of birefringence was observed
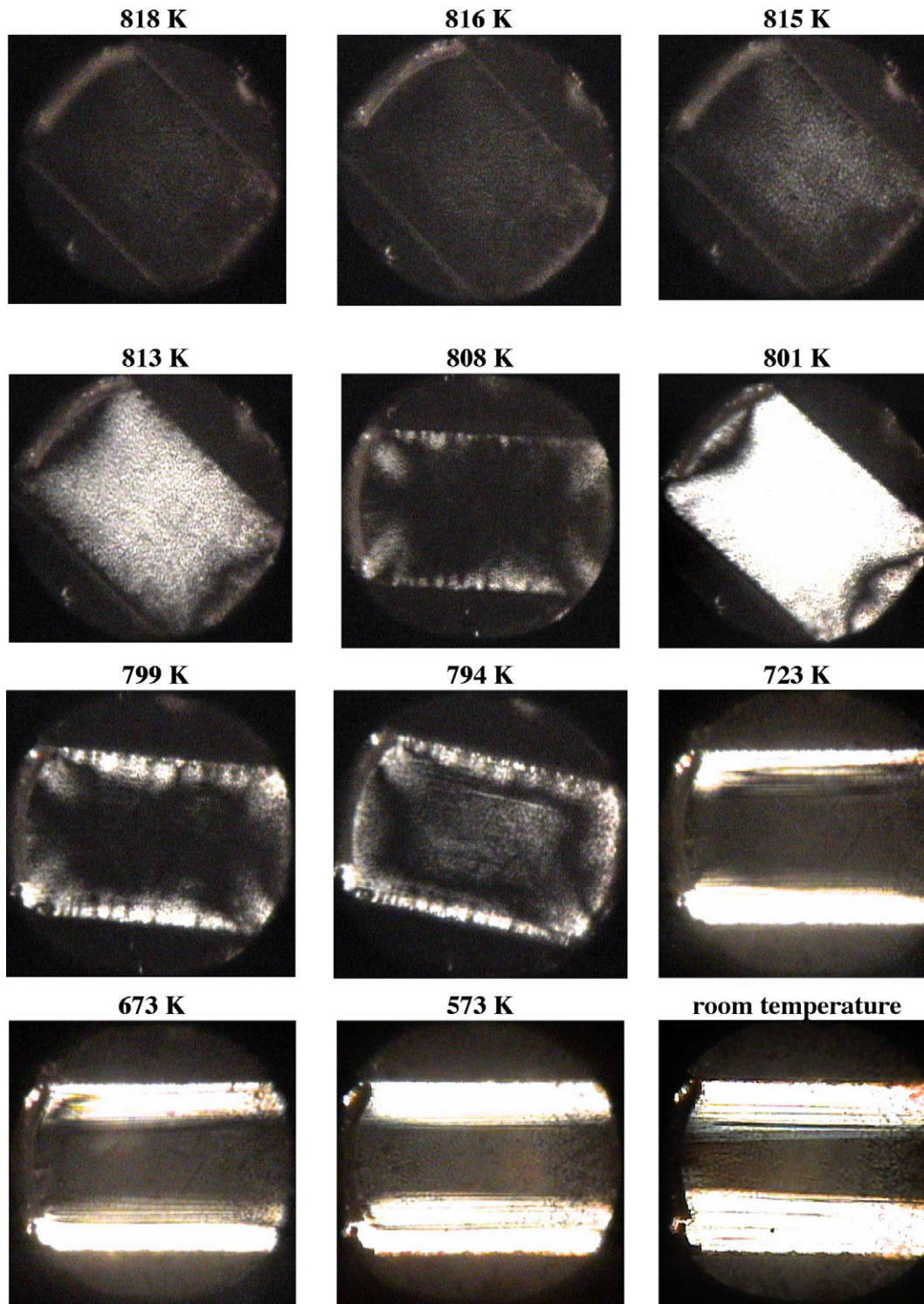
Figure 11. A representative set of optical micrographs showing variations of microstructure with temperature in the (110) plate. These were obtained *in situ* within the Brillouin spectrometer, with the crystal held between (E–W and N–S) crossed polars. In the micrographs recorded at 818, 816, 815, 813 and 801 K the crystal was in the 45° position. In the micrographs recorded at 723, 673, 573 K and room temperature, the central portion of the crystal was in its extinction position while twins along the edges were not. Micrographs collected at 808, 799 and 794 K were obtained at intermediate angles to reveal a complex pattern of weak birefringence associated with the edges of the crystal. This is interpreted as being due to local strain effects. Note that the trace of a twin wall parallel to the length of the crystal is visible in the upper part of the micrograph collected at 794 K but not in the micrograph obtained at 799 K.

when the crystal was rotated through 45° to the nominal extinction position. This is illustrated in the 811 K micrograph of figure 12 and suggests a degree of non-uniform strain

across the plate. At 788 K (figure 12) this pattern was gone. At all lower temperatures the predominant texture was of parallel twins dominating in one direction (parallel to (010)
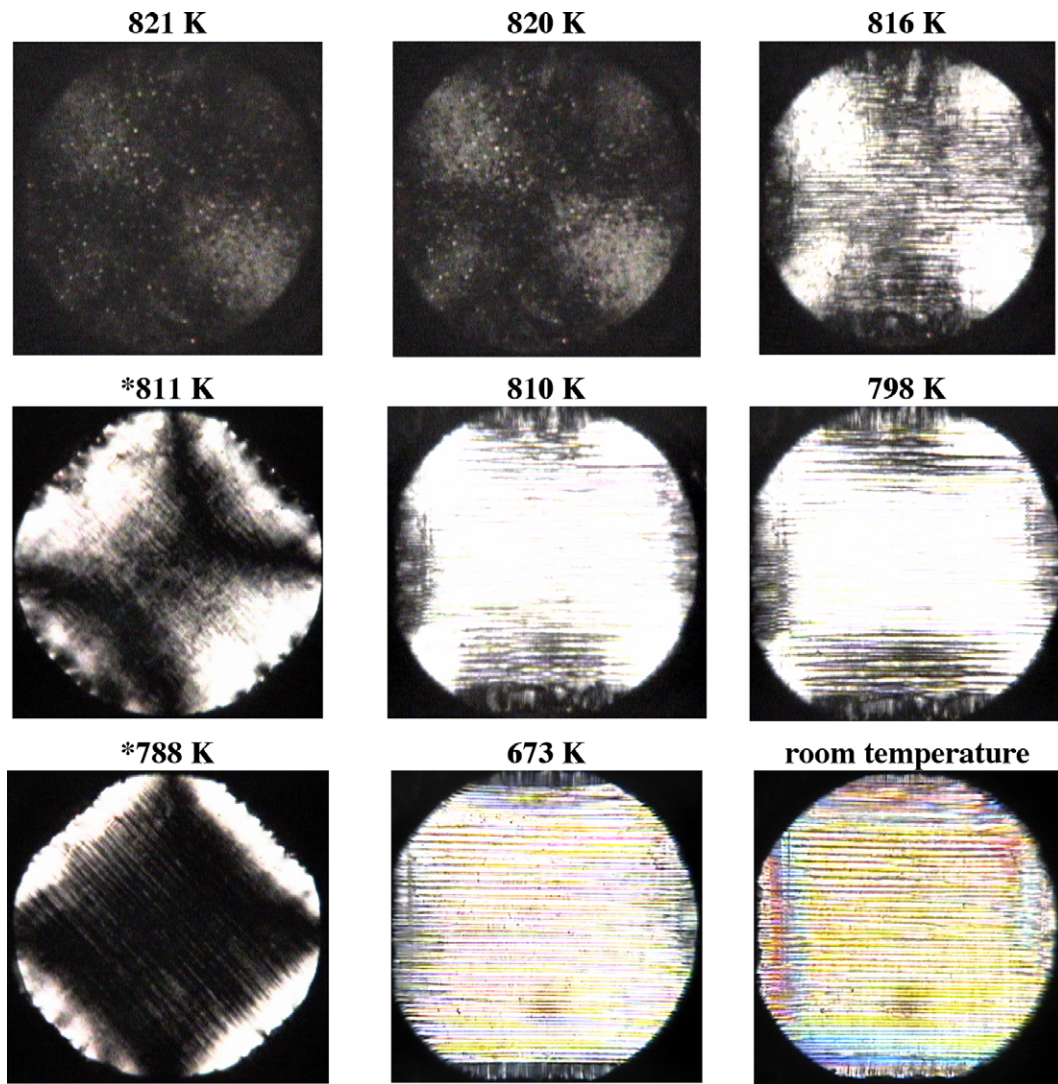
Figure 12. A representative set of optical micrographs showing variations of microstructure with temperature in the (100) plate. 811 and 788 K micrographs (indicated by an asterisk) were collected with the crystal in its extinction position. In the micrographs obtained at other temperatures, the crystal was in the 45° position, showing maximum birefringence. Speckling in some images is due to dirt accumulating on the windows of the sample holder.

in figure 12), though with traces of a second twin orientation always visible. As with the (110) plate, the microstructures at high temperatures were reproducible during heating and cooling. Some changes occurred in the spacings of twins observed at room temperature before and after heating to high temperatures.

These observations of microstructural evolution are rather similar to those described by Hayward *et al* (2005). The (110) and (100) slices used for quantitative birefringence measurements (Hayward *et al* 2005) were from the same batch as prepared for the experiments described here. Close correspondence between the two sets of data should be expected, therefore. Hayward *et al* (2005) found a uniform decrease in retardation in a portion of their (100) plate away from strained regions, with a deviation from linearity between 830 and 750 K. This reduced to zero at 830 K. They reported the appearance of twins as occurring below ∼820 K, with the persistence of weak birefringence up to at least 825 K. The

(110) plate contained no obvious twin walls and the optical retardation decreased uniformly with increasing temperature. A change in slope was observed at ∼720 K, and an unusual crossover from positive to negative retardation was found at 802 K. Their data are reproduced in figure 8 showing how this negative retardation reached its greatest magnitude at 820 K before returning to zero at ∼830 K. If the absolute minimum in the retardation at 820 K corresponds with the transition temperature of 817 K considered here, the crossover at 802 K would correspond almost exactly with the lower temperature limit (∼797 K) of the 20 K interval in which a complex pattern of elastic properties has been found. Hayward *et al* explained the crossover as being due to an adjustment in the relative proportions of twins with different optical orientations, separated by twin walls within the plane of the plate. However, the only twin walls parallel to (110) would separate type I ($\bar{3}$ axis ∥ [111]) and type IV ($\bar{3}$ axis ∥ [$\bar{1}\bar{1}1$]) twins (see figure 1 of Carpenter *et al* 2010b). The optical indicatrix of

each of these two twins would have the same orientation, so that changing their volume proportions would not give the reversal of retardation actually observed. Nevertheless, it is clear from the present study that substantial changes in twin configuration do take place within (110) plates above ∼750 K.

6. Discussion

Octahedral tilting transitions in perovskites can be understood at one level as being due to a single driving mechanism, namely a zone boundary soft mode involving the motions of more or less rigid octahedra. However, from the diversity of sequences of structures in transformation hierarchies, wide variations in the thermodynamic character of nominally the same transition in different perovskites and the failure of most theories to reproduce subtle variations in physical properties related to the order parameter, this must be an oversimplification. In the present study, attention has been focused on the evolution of properties which depend on the order parameter susceptibility. The most immediate general result discussed below is that a classical Landau treatment of the elastic softening in terms of a static order parameter is successful over a wide temperature interval away from the transition point but is inadequate over a temperature interval of ∼100 K below T_c (figure 6). The new Brillouin data include information on dynamical/relaxational effects which can be responsible for the deviations and these form the main focus of the rest of the discussion presented here. Softening as $T \rightarrow T_c$ within the stability field of the cubic phase is discussed in detail in Carpenter *et al* (2010a).

6.1. Observed and calculated elastic softening in the $R\bar{3}c$ field

Figure 6 contains experimental data for individual elastic moduli, from Brillouin spectroscopy (this study) and RUS (Carpenter *et al* 2010a), together with variations calculated on the basis of the classical Landau model. Linear trends for the bare elastic moduli C_{11}^o, C_{12}^o and C_{44}^o were obtained by fitting to RUS data from the cubic structure in the temperature interval 855–1036 K, to exclude the interval of softening as $T \rightarrow T_c$. These fits were used also to calculate linear trends for K° ($=\frac{1}{3}(C_{11}^o + 2C_{12}^o)$) and $\frac{1}{2}(C_{11}^o - C_{12}^o)$. Hill values of the shear modulus (average of Voigt and Reuss limits) were calculated from C_{11}^o, C_{12}^o and C_{44}^o in the usual way and a straight line was fit to the data over the same limited temperature interval in order to determine the temperature dependence of G°. Changes in single crystal elastic moduli due to the $Pm\bar{3}m \rightarrow R\bar{3}c$ transition were calculated using the equations in table 2 and the set of coefficients in table 3, and then subtracted from the linear extrapolations of C_{11}^o, C_{12}^o and C_{44}^o. Finally, single crystal elastic moduli for the $R\bar{3}c$ structure with standard reference axes of a trigonal system were determined using the expressions in table 1 of Carpenter *et al* (2010b), and Hill values of K and G then calculated from these using expressions given by Watt and Peselnik (1980). Most of the Landau coefficients were obtained independently of the elastic moduli. Agreement between observed and calculated values of C_{44}, in particular, is therefore a measure of the adequacy of the model to describe the elastic softening. It

was necessary to adjust the values of λ_1 and λ_2 to produce fits to K and $\frac{1}{2}(C_{11} - C_{12})$ at room temperature, so that variations of some of the other moduli do not provide such an independent test of the model. Nevertheless, it is clear that close agreement is obtained between observed and calculated elastic moduli for a wide temperature interval in the $R\bar{3}c$ stability field. Poorest agreement is for C_{36}, which has observed and calculated values at room temperature of -25 and -20 GPa, respectively. The final, preferred value of $\lambda_1 = -0.59$ GPa lies between -0.42 extracted from the pressure dependence of the transition temperature and -1.14, extracted from the variation of e_1. Note that the latter value was quite poorly constrained because of uncertainties in the extrapolation of the cubic lattice parameter, a_o.

Between ∼700 and 817 K there are distinct and systematic deviations of the elastic moduli from the predictions of Landau theory. The largest difference occurs for C_{44} (and, hence, also for G), and the smallest is for C_{12} and K. From the perspective of a purely classical description of elastic relaxations, as set out in sections 2 and 3 above, these anomalies might be due to variations of the strain/order parameter coupling coefficients, λ_i, and/or the coefficients a, b, b'. If the additional softening was due simply to increases in the values of λ_i, there should be associated increases in the magnitude of the spontaneous strains relative to the trends established at lower temperatures. Data for e_4 show that the reverse is actually observed, however, with lower than expected values between ∼700 K and T_c (figure 1(a)), and there is no obvious change in the trend of e_1 (figure 1(b)). Changes in the coupling coefficients can probably be ruled out, therefore.

Absolute values of a and $(3b^* + b'^*)$ for the Landau description were set using heat capacity data but alternative values of a seem unlikely to be responsible for the extra softening. For example, increasing a to 0.000 13 GPa leads to additional softening of C_{44}, $\frac{1}{2}(C_{11} - C_{12})$ and K by only ∼1– 2 GPa (table 5). Reducing a to 0.0001 GPa reduces the amount of softening to a similar extent. On the other hand, there is clear evidence for variations of the order parameter susceptibility in the evolution of the soft mode frequencies. In particular, the ratio $3\omega_E^2/(\omega_A^2 + 2\omega_E^2)$ has a maximum at ∼300 K (figure 3(d)) and would fall to zero at ∼760 K if ω_E^2 really extrapolated to zero as shown in figure 3(b). At 0 K and ∼700 K, it is ∼0.152 and ∼0.12 respectively. These three alternative values have been used to redetermine values of b^* and b'^* in order to propagate their influence through to the elastic moduli. The resulting variations are listed in table 5. Changing the $b^*:b'^*$ ratio according to the ratio of soft mode frequencies in this way (at constant $(3b^* + b'^*)$) produces increases in softening of C_{44} and $\frac{1}{2}(C_{11} - C_{12})$ as $T \rightarrow T_c$. Thus the additional softening could be due a temperature dependence of the susceptibilities which arises mainly from a reduction in the value of b'^* (equation (27)). If the coupling coefficients are constant, the underlying trend might therefore be explained in terms of a reduction in the effective value of b' as $T \rightarrow T_c$. This cannot be the only factor, however, as reducing b'^* to zero produces softening of C_{44} which is less than observed at 793 K and softening of $\frac{1}{2}(C_{11} - C_{12})$ which is greater than observed (table 5).

Table 5. Calculated changes of selected elastic moduli, in units of GPa, due to the cubic–rhombohedral phase transition for different model parameters (with $\lambda_1 = -0.59$, $\lambda_2 = -0.32$, $\lambda_3 = 1.17$ GPa). For the different values of $3\omega_E^2/(\omega_A^2 + 2\omega_E^2)$, a was held at 0.000 117 GPa and $(3b^* + b'^*)$ at 0.286 96 GPa. Observed softening values were given by the difference between the linear baselines shown in figure 6 and the values of the elastic moduli obtained by Brillouin scattering.

	b^*	b'^*	b	b'	ΔC_{44}	$\Delta\frac{1}{2}(C_{11}-C_{12})$	ΔK	C_{46}	C_{36}	C_{24}
a										
0.000 1	0.076 58	0.015 35	0.084 50	0.019 85	−17	−37	−8	4	−21	18
0.000 117	0.089 66	0.017 98	0.097 58	0.022 47	−16	−35	−7	4	−20	17
0.000 13	0.099 56	0.019 96	0.107 48	0.024 45	−15	−33	−6	3	−19	15
$\dfrac{3\omega_E^2}{\omega_A^2 + 2\omega_E^2}$										
0 (∼760 K)	0.095 65	0	0.103 58	0.004 49	−29	−70	−7	10	−45	29
0.12 (∼700 K)	0.091 49	0.012 48	0.099 42	0.016 97	−18	−41	−7	5	−24	19
0.152 (0 K)	0.090 26	0.016 18	0.098 18	0.020 67	−16	−36	−7	4	−21	17
0.167 (295 K)	0.089 66	0.017 98	0.097 58	0.022 47	−16	−35	−7	4	−20	16
Unrenormalized susceptibility	0.095 41	0.000 74	0.103 33	0.005 23	−28	−67	−7	4	−20	17
Observed										
$T = 295$ K					−16	−35	−7	4	−25	15
$T = 723$ K					−22	−37	−9	7	−23	15
$T = 793$ K					−47	−45	−11	17	−29	7

A further consideration is in the choice of renormalized versus unrenormalized order parameter susceptibilities, i.e. those derived from equation (11) rather than from equation (1). The ratio $\omega_E^2/\omega_A^2 = 0.0581$ from figure 3(c) has been used in equation (28) to derive values for b and b' for the unrenormalized case. This produces essentially the same numerical results as obtained from setting $3\omega_E^2/(\omega_A^2 + 2\omega_E^2) = 0$ for the renormalized susceptibility (table 5), and the effect is again attributable to reducing the value of b'. In physical terms such a crossover would imply a change in relative relaxation times. When equation (21) is used to calculate elastic softening associated with a phase transition, the implicit assumption is that the order parameter responds instantaneously to a change is strain state. This will generally be the case for a displacive transition. The reverse is not necessarily the case, however, in that the timescale for relaxations of local strain states need not be short in relation to the timescale of a change in the order parameter. If the response times are comparable, then the susceptibilities derived from the fully renormalized Landau expansion effectively control the softening. If, on the other hand, the response time of the structure to changes in strain becomes significantly longer than the timescale on which changes in Q occur, (the phonon timescale), susceptibilities derived from the unrenormalized expansion would control the effective softening. Underlying this issue is the nature of coupling between acoustic modes and the soft optic mode, plus any damping.

The additional elastic softening beyond that expected on the basis of Landau theory can be related at least in part to an effective reduction in the value of the b' coefficient at high temperatures. This has an additional consequence in relation to the development of the Brillouin central peak. The R-point instability in perovskites can give rise to structures with space group $I4/mcm$, $Imma$ or $R\bar{3}c$. Using a Landau expansion of the form of equation (1) gives the well-known stability criteria for these structures (Thomas and Müller 1968, Harley *et al* 1973, Birgeneau *et al* 1974, Darlington 1997, Carpenter 2007)

as $R\bar{3}c$ being the stable form for $b'^* > 0$ and $I4/mcm$ the stable form for $b'^* < 0$. The $Imma$ structure is expected to be intermediate between these but should have the same energy when $b'^* = 0$. In other words, for small values of b'^*, the energy barrier for transforming between them becomes small and, at some point, it must be expected that fluctuations of the octahedral tilt axis will develop between $\langle 111 \rangle$ for the $R\bar{3}c$ structure, $\langle 011 \rangle$ for the $Imma$ structure and $\langle 001 \rangle$ for the $I4/mcm$ structure.

6.2. Dynamic central peak and acoustic mode coupling

The appearance of a central peak is a common feature of Brillouin, Raman and inelastic neutron scattering spectra obtained from crystals held at temperatures close to a structural phase transition. The development of the central peak is usually accompanied by elastic softening and anelastic dissipation effects which are additional to those expected on the basis of classical strain/order parameter coupling. A diversity of mechanisms has been proposed in relation to the origin of this quasi-elastic scattering, including the influence of fluctuations, clusters, domains, ionic mobility and defects (Fleury and Lyons 1979, 1981, 1983). The central peak provides evidence of additional relaxation processes which can couple with the optic and/or acoustic modes of the crystal. Information as to the precise nature of the relaxation processes involved is contained in details of how the width and intensity of the central peak evolve with temperature through the transition point. For LaAlO₃, the most important feature in this context is, firstly, that the central peak is observed only in the stability field of the $R\bar{3}c$ structure. If precursor clustering or local regions of dynamic order exist within the cubic phase they evidently do not give rise to a central peak. This represents an extreme contrast from PLZT relaxors, say, in which polar nanoregions are believed to be responsible for a central peak which decays over a temperature interval of ∼200 K above

a diffuse transition point (Shabbir and Kojima 2004, Ko *et al* 2006a, 2006b). It is, however, the expected result for central peak behaviour due to phonon density fluctuations at an improper ferroelastic phase transition in which the low symmetry phase is neither ferroelectric nor piezoelectric (Cowley and Coombs 1973). Secondly, the appearance of the central peak is clearly accompanied by broadening and reductions in Brillouin shift of all the acoustic modes of the $R\bar{3}c$ structure, irrespective of the direction in which they were measured. There appears to be coupling of the central peak mode with all the acoustic modes, therefore. Finally, the maximum amplitude of the central peak and maximum values of the LA and TA linewidths occur at ∼10–15 K below the transition point for [00$\bar{1}$] and [1$\bar{1}$0] directions within the (110) plate and [011] within the (100) plate. This differs from the characteristic pattern of critical slowing down associated with order/disorder behaviour and bilinear coupling of the order parameter with a symmetry breaking strain, in which a maximum in the attenuation would be expected at $T \approx T_c$ of a second order phase transition (Landau and Khalatnikov 1954, Rehwald 1973).

A full mode–mode coupling analysis for LaAlO$_3$ is beyond the scope of the present paper. Instead, a multi-peak fitting routine in the software package IGOR (Wavemetrics Inc, Oregon) has been used to provide a relatively simple and semi-quantitative assessment of peak widths and peak heights in the Brillouin spectra. Selected spectra were first analysed by fitting with individual Lorentzian peaks. These provided satisfactory agreement with the observed intensities, as illustrated in figure 13, except that problems were encountered with correlation of fit parameters when the TA$_2$ and central peaks overlapped to a substantial degree. More robust fitting, i.e. with the least correlation between fit parameters, was obtained using Voigt profiles and this approach was therefore applied systematically to all the spectra. Data for the full width at half maximum height, Γ, of all the peaks in spectra collected for the [00$\bar{1}$] direction of the (110) plate are shown in figure 14(a), together with the heights of the central peak. It should be emphasized that these results are only semi-quantitative because parameters for the central peak were obtained from its lateral variations away from the central portion of each spectrum which was blocked by the shutter in the spectrometer.

Between ∼650 K, when the central peak can first be detected, and ∼790 K, Γ for the central peak appears to remain approximately constant or only weakly temperature dependent. The fitted peak then becomes narrower, before broadening again. Its intensity increases steadily to a maximum at ∼802 K, where Γ is at a minimum, before decaying more rapidly to zero close to $T \approx T_c$. A Lorentzian profile would be expected for a Debye-type relaxational process, in which case the relaxation time, τ, is given by (Ko *et al* 2006a, Tsukada *et al* 2007, 2008, Mączka *et al* 2008)

$$\tau = \frac{1}{\pi\Gamma}. \tag{32}$$

On this basis, the calibration of frequency shift with acoustic velocity gives relaxation times of between ∼10 and 100 ps (figure 14(b)). Lorentzian fits to the data gave a similar range of relaxation times. Note that the trend of reducing 1/(central
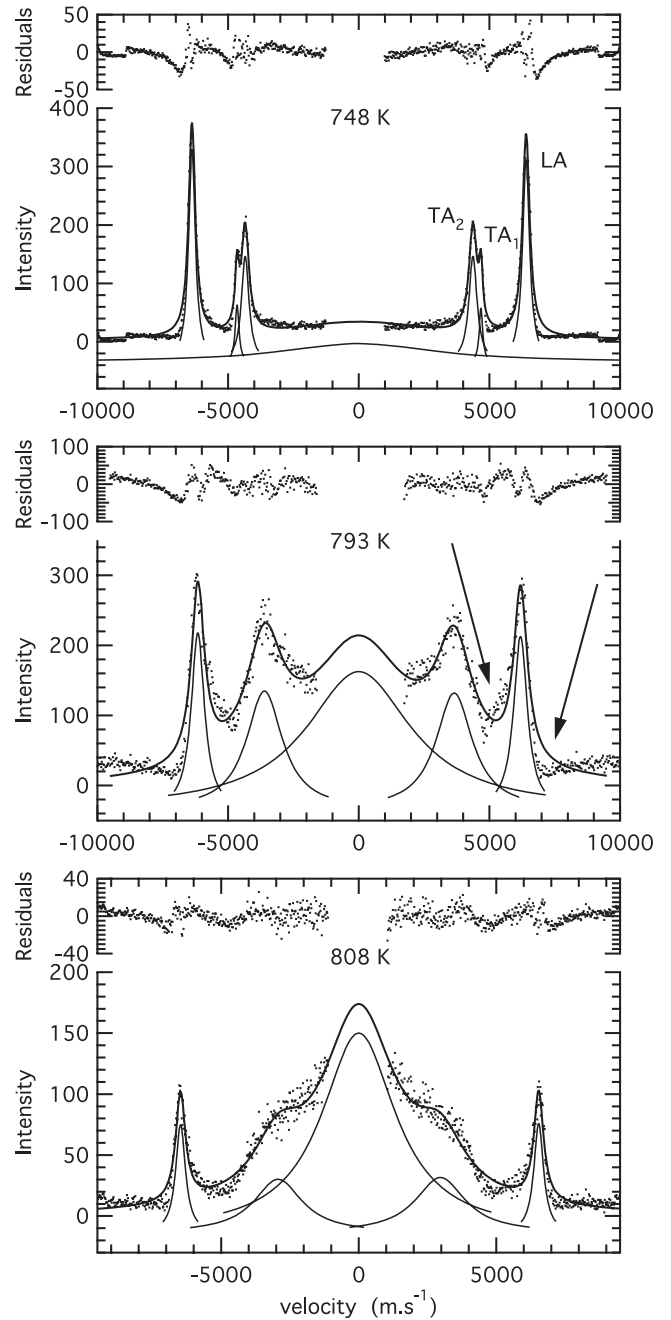

Figure 13. Representative examples of fits to experimental data for direction [00$\bar{1}$] in the (110) plate using Lorentzian profiles to represent the central peak, LA- and TA-peaks. Dots are data and continuous solid lines are the fits. Individual peaks from the fitting are also shown, slightly displaced, below the spectra. Arrows indicate the gain of intensity on the low velocity side of a peak and the loss of intensity on the high velocity side which is a characteristic feature of coupling of individual modes with the central peak mode.

peak height) from the fitting procedure for temperatures close to T_c is also seen in an equivalent plot of the intensity data measured close in to the centre of the primary spectra over a wider temperature interval (figure 14(c)).

Changes in relaxation times close to structural phase transition are usually discussed in terms of crossover from displacive to order/disorder behaviour. Some examples of this are the proper ferroelastic transitions in BaTi$_2$O$_5$ (Hushur
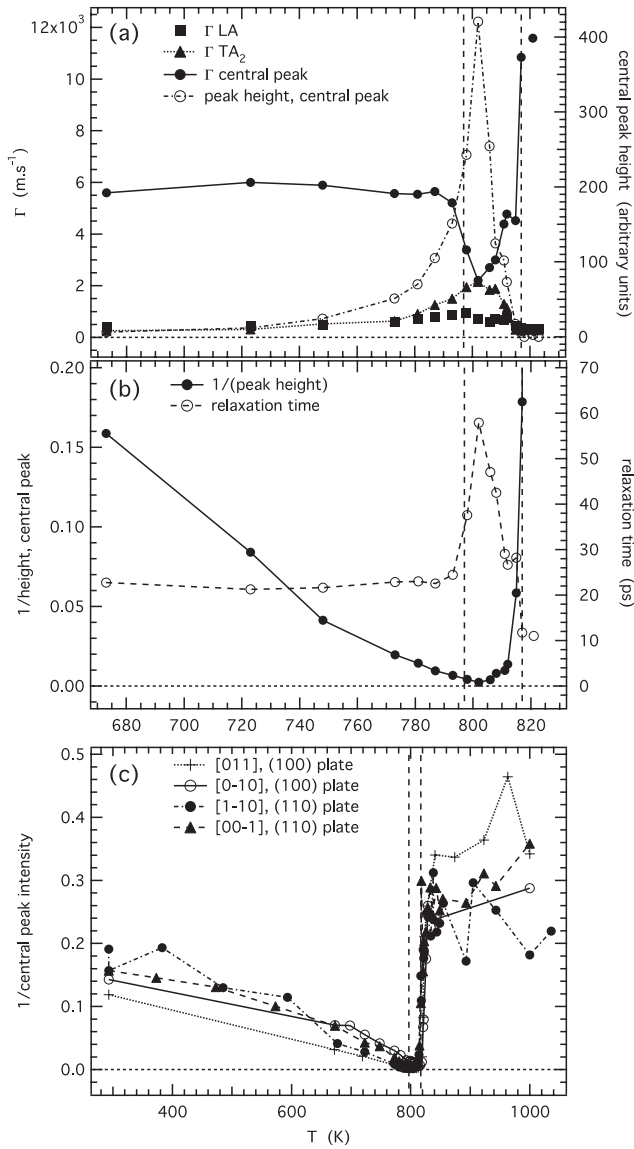
Figure 14. (a) and (b) contain parameters extracted from fits of the type shown in figure 13 (though using Voigt instead of Lorentzian peak profiles) for direction [00$\bar{1}$] in the (110) plate, while (c) contains data from the primary spectra. (a) The full width at half maximum height, Γ, of the central peak (left axis) is more or less constant below ~797 K before dropping to a minimum at ~802 K and then increasing towards 817 K. There is a corresponding maximum in the intensity of the central peak at ~802 K (right axis). Γ for LA and TA$_2$ peaks (left axis) shows increasing peak widths as temperature increases towards ~797 K, irregular variations between ~797 and 817 K followed by an abrupt drop to small values above 817 K. (b) Variations of the inverse of the height of the central peak (left axis), which appears to behave like a susceptibility, and of the relaxation time for the central peak mode (right axis), determined from the width of the central peak. Changes in the relaxation time between ~797 and ~817 K are ascribed to the influence of a flip mode. (c) The inverse of the central peak intensities given in figure 7, as measured close in to the centre of the primary spectra.

et al 2005) and hexagonal BaTiO$_3$ (Yamaguchi *et al* 1995), the ferroelectric transition in LiTaO$_3$ (Hushur *et al* 2007), and the incommensurate phase transition in Ba$_2$NaNb$_5$O$_{15}$ (Zhang *et al* 1986). Critical slowing down in the order/disorder limit is generally expected to follow the Landau–Khalatnikov relation

(Landau and Khalatnikov 1954)

$$\tau = \frac{\tau_o T_c}{|T - T_c|},\tag{33}$$

where τ_o is a constant and T_c is the transition temperature. In the present case the apparent changes in relaxation time from the central peak define approximately linear trends on either side of the minimum in Γ at ~802 K. They could then imply some order/disorder process centred on ~802 K. Central peak widths and heights extracted from fitting of Voigt peaks to spectra for other crystallographic directions showed more scatter, though they confirmed the general pattern of peak heights suggested by the data in figure 7. They were also consistent with a tendency for the narrowest central peaks (shortest relaxation times) to occur within the ~797–817 K interval.

Broadening of the LA and TA$_2$ peaks is accompanied by the development of distinct asymmetry in the peak profiles (figure 13). Intensity is lost from the high velocity side of each peak and gained on the low velocity side. This is a characteristic consequence of coupling with the central peak mode (e.g. Katiyar *et al* 1971, Oliver *et al* 1988). The broadening reaches a maximum for the TA peak at the same temperature as the central peak achieves maximum intensity and minimum width (figure 14(a)). Line broadening and additional softening of the LA mode is lesser in magnitude but similar in form. As far as can be deduced from the present study, therefore, the strength of coupling between the central peak and all the acoustic modes reaches a maximum ~5–15 K below T_c but diminishes with increasing frequency difference. On this basis, the coupling could then also account for the change in linewidths of the LA- and TA-peaks (figure 14(a)).

The TA$_1$ peak for the [00$\bar{1}$] direction in (110) reduces in intensity with increasing temperature and is not discernible in spectra collected above ~785 K (see figure 13). This is consistent with the overall pattern of spectra discussed above which implies that the structure of LaAlO$_3$ is tending towards becoming effectively cubic on a local phonon length scale in the ~797–817 K interval.

In summary, this simple fitting procedure (independent modes, Voigt profiles, no consideration of instrumental contributions to linewidth, attribution of all central peak intensity to a single mode) provides evidence in support of the view that additional softening of the elastic moduli beyond the predictions of classical strain/order parameter coupling in LaAlO$_3$ is due to coupling between the acoustic modes and a dynamical central peak mode. In terms of bulk physical properties, the influence of this coupling is seen in both the shear and bulk moduli, but is stronger for the former than for the latter (figure 6). The question then remains as to the actual mechanism of the central peak mode. Unlike most of the systems with central peaks reviewed by Fleury and Lyons (1983), (to which may be added: PbTiO$_3$, Hellwig *et al* 2003; LiTaO$_3$, Hushur *et al* 2007; Ba$_2$NaNb$_5$O$_{15}$, Oliver *et al* 1988, 1990, Scott and Oliver 1990; K$_3$Nb$_3$O$_6$(BO$_3$)$_2$, Mączka *et al* 2008; hexagonal BaTiO$_3$, Yamaguchi *et al* 1995, Jiang and Kojima 2000a, 2000b; BaTi$_2$O$_5$, Hushur *et al* 2005; KNbO$_3$ and BaTiO$_3$, Sokoloff *et al* 1988; Ta$_{1-x}$Nb$_x$O$_3$, Sokoloff *et al*

1990; Cs$_2$CdBr$_4$, Kuzel *et al* 1994; and diverse relaxors, e.g., Siny *et al* 1997, 2001, Jiang *et al* 2002, Fan *et al* 2002, Shabbir and Kojima 2004, Kim *et al* 2005, Shabbir *et al* 2005, Tsukada *et al* 2006, Ko *et al* 2006a, 2006b, 2006c, 2007a, 2007b, Shabbir and Kojima 2007, Ko and Kojima 2007), LaAlO$_3$ is believed to be neither ferroelectric nor piezoelectric. The only analogous improper ferroelastic phase transition at which a central peak has so far been reported occurs in SrTiO$_3$ (Lyons and Fleury 1977, Fleury and Lyons 1979, 1981, 1983). Lyons and Fleury (1977) examined Brillouin spectra for one crystallographic direction and observed a central peak with $\Gamma \approx 20$ GHz in a temperature interval from <1 K above T_c to ~ 7 K below T_c, with a maximum in the intensity occurring at $(T_c - T) \sim 1.5 \pm 0.6$ K. Fitting of the central peak using a relaxational model led them to identify two relaxation processes, one with a relaxation time of ~ 70 ps and the second with a relaxation time of ~ 3 ns. They concluded that their observed central peak arises from coupling of the soft optic mode with a subset of the fluctuations in phonon density which occur at $T < T_c$.

Following the works of Lyons and Fleury (1977) for the specific case of SrTiO$_3$ and Coombs and Cowley (1973), Cowley and Coombs (1973) for a more general treatment of the influence of fluctuations, a working hypothesis for the underlying mechanisms giving rise to the central peak mode behaviour in LaAlO$_3$ is now proposed. According to Cowley and Coombs (1973), the zone boundary soft optic mode is not expected to couple with fluctuations of the phonon density above T_c but should display the characteristics of a classically damped harmonic oscillator. A central peak has been observed in inelastic neutron scattering spectra as $T \rightarrow T_c$ and was treated in terms of the soft mode becoming critically overdamped (Axe *et al* 1969, Kjems *et al* 1973). At $T < T_c$, the soft mode can couple with fluctuations of the phonon density to give rise to the central peak in Brillouin spectra. Below ~ 797 K the central peak mode appears to have a more or less constant relaxation time and gives rise to a peak height (as a proxy for integrated intensity) which diverges in a manner which is not far from $(T_o - T)^{-1}$ (figure 14(b)). If this divergence was followed exactly, it would be the same as expected for the order parameter susceptibility at a second order transition, except that T_o (~ 802 K) is ~ 15 K below T_c. In detail, the inverse of the intensity does not vary exactly linearly with temperature and tends to a minimum at ~ 805 K rather than at 817 K (figure 14(b)). This pattern seems to match the evolution of the soft mode frequencies, however, which also appear to trend towards zero well below T_c; both may be reflecting the true order parameter susceptibility of the system as modified by the influence of the phonon density fluctuations.

In the temperature interval ~ 797–817 K, a quite different pattern of evolution for the apparent relaxation time and central peak intensity suggests a change in mechanism. One possibility is the development of a 'flip mode' analogous to the interpretation offered by Salje *et al* (1983) for the appearance of an apparently intermediate phase at the rhombohedral $\rightarrow$ monoclinic phase transition in Pb$_3$(PO$_4$)$_2$ and Pb$_3$(P$_{0.77}$As$_{0.23}$O$_4$)$_2$. The order parameter for the transition in Pb$_3$(PO$_4$)$_2$ is due to the condensation of a soft mode which

results in displacements of Pb atoms away from a three-fold symmetry axis. Over a temperature interval which extends down to ~ 20 K below the transition point, there is also the possibility of flipping of the monoclinic twin axes between three different orientations. Salje *et al* (1983) reported a relaxation time of ~ 30 ps for their flip mode, which falls in the range of apparent relaxation times indicated in figure 14(b). In LaAlO$_3$, the order parameter relates to the average tilt angle of octahedra rotated about a single direction belonging to $\langle 111 \rangle$. Clusters of tilted octahedra could flip between the four twin orientations so long as the energy barrier between them was low. More likely is flipping between tilt axes along $\langle 111 \rangle$, $\langle 011 \rangle$ and $\langle 001 \rangle$, as would occur readily for free energy wells determined by small values of b'^* in equation (11). The frequency and intensity of this flip mode would be expected to vary with the magnitude of the energy barrier, perhaps reaching a crossover point at some $T < T_c$, below which it would start to decline. The ~ 797–817 K interval found here for elastic behaviour which is intermediate between that of the $R\bar{3}c$ and $Pm\bar{3}m$ structures would then correspond to the temperature interval over which the strongest fluctuations develop (and within which there is a small additional excess in the heat capacity, cf. figure 2). The flip mode would have properties analogous to those of a phonon in terms of its coupling behaviour, though it could have characteristics of an order/disorder process. It would also cause the local average structure to appear to be cubic, depending on the sampling length and timescale. As a final aside, such a flip mode would behave differently within twin domains and within twin walls, giving rise to some microstructural control of its intensity and influence.

6.3. The role of microstructure

Chrosch and Salje (1999) found significant and strongly temperature dependent intensity between Bragg positions in single crystal x-ray diffraction patterns from a twinned crystal of LaAlO$_3$, which they interpreted in terms of increasing twin wall thickness, w, as $w \propto (T_c - T)^{-1}$. The twin wall thicknesses reach ~ 200 Å near T_c. Any correlation with the temperature dependence of the intensity of the central peak does not necessarily imply that the two effects are directly related but three observations suggest that the twin walls may be a contributory factor to the central peak behaviour, at least in the 797–817 K interval. Firstly, there is the difference in the temperature at which the intensity of the Brillouin spectrum in the quasi-elastic scattering region reaches a maximum in the [00$\bar{1}$] and [0$\bar{1}$0] directions (figure 7). The principal physical difference between the two plates from which these spectra were collected is that there was no visible microstructure in the (110) plate between ~ 797 and 817 K, whereas a distinctive cross-hatch pattern of twins remained in the (100) plate (figures 11 and 12). Secondly, values of the elastic moduli derived from the LA acoustic mode velocity for these two directions should be the same under $\bar{3}m$ and $m\bar{3}m$ symmetry, but they are observed to be different (figure 8). The value of the modulus for the [00$\bar{1}$] travel direction was obtained from the apparently twin free (110) plate and is actually the

same as would be expected if the low temperature data were extrapolated to high temperatures without any of the additional softening. The implication is that the additional softening of the LA mode for $[0\bar{1}0]$ in the twinned (100) plate could be due to the influence of the fine scale twins. These twins have wall thicknesses of $\sim$150–200 Å by this stage, according to the results of Chrosch and Salje (1999). Thirdly, there was a change in microstructure of the (110) plate as a consequence of the first heating cycle through T_c and the spectrum collected at 805 K during heating was different from that collected during cooling. This apparent hysteresis could be accounted for if the initial twinning texture of the plate was inherited from the large single crystal from which it was cut but did not return when it was cooled through T_c as a thin slice.

In a large single crystal, there is presumably an isotropic distribution of twin orientations. As evidenced by the images in figures 11 and 12, this is clearly not the case for thin plates and the most obvious cause of the difference would be strain fields arising from relaxations of the structure penetrating in from the surfaces. Direct evidence for the dimensions of such strain fields is provided by the birefringence patterns seen along the long edges of the (110) plate at 794, 799 and 808 K (figure 11). The width of these is $\sim$40–50 μm. In the (100) plate, the strained birefringent regions penetrating in from the edges are $\sim$100 μm wide at 785 K. If they extend into the crystal from the polished top and bottom faces by similar amounts, a substantial proportion of the total volume of the 190 μm plates would be affected. The patterns of birefringence between $\sim$800 K and T_c also suggest strain fields emanating from the corners of the plates. Either because of its symmetry or because of its square shape, these patterns of birefringence suggest a uniaxial stress field existing in the (100) plate, which presumably allows the symmetrical distribution of cross-hatched twins to remain. The (110) plate would have had a less symmetrical stress distribution, which may have been a contributory factor in the disappearance of twin walls.

Finally, twin walls in the (100) plate had their traces parallel to [001] and/or [100] at all temperatures, including at 797–817 K. If there was an intermediate phase with tetragonal symmetry (e.g. $I4/mcm$, $b'^* < 0$), then {110} twins would be expected instead. Thus, although the microstructure in the (100) plate is different in scale over the intermediate temperature range, it is consistent with the $Pm\bar{3}m \leftrightarrow R\bar{3}c$ transition occurring at $T_c \approx 817$ K.

6.4. Anomalies in structural parameters

As well as presenting new information from a variety of experimental techniques relating to changes in structure and properties due to the $Pm\bar{3}m \leftrightarrow R\bar{3}c$ transition in LaAlO₃, Hayward *et al* (2005) summarized previous results from the literature and concluded that there is a distinct break in the evolution of many properties at $\sim$730 K as well as at $T = T_c$. In particular, the octahedral tilt angle, ϕ, and the octahedral distortion parameter $(1 - \eta)$ obtained from structure refinements of neutron powder diffraction data do not follow the order parameter, q, in the manner predicted

for a second order phase transition, i.e. $(1 - \eta) \propto \phi^2 \propto q^2 \propto (T_c - T)$. Hayward *et al* (2005) suggested that the deviations from classical second order behaviour can be understood in terms of biquadratic coupling between two discrete order parameters, the first being due to the octahedral tilt instability and the second being due to clustering of oxygen vacancies. This mechanism will give breaks in slope of the temperature dependence of both order parameters if the two critical temperatures are different. Extrapolation of the temperature dependent trends of structural data from low temperatures should then give apparently different values of T_c from the actual value obtained, say, by measurements of heat capacity. Crucially, however, the spontaneous strains (as replotted in figure 1 above) extrapolate to zero at $T = T_c$, even though the evolution of e_4 perhaps becomes anomalous above $\sim$650 K. Similarly, there is no obvious break in slope of the twin angle as a function of temperature in the data reported by Chrosch and Salje (1999).

If the view is taken that anomalous behaviour is associated essentially with the order parameter susceptibility, through variations in the soft mode frequencies and elastic moduli, an alternative explanation of the structural evolution described by Hayward *et al* (2005) is that coupling of a single order parameter occurs with a second relaxation process rather than with a second order parameter. Some reconsideration of the structure refinements, to separate static from dynamic contributions in neutron diffraction patterns, might clarify the origin of deviations in the evolution of ϕ and $(1 - \eta)$ if the relaxation process involves phonon density fluctuations. Whether such dynamical effects and/or associated variations in microstructure and strain fields in thin plates could be responsible in detail also for the variable trends in optical birefringence found by Hayward *et al* (2005) remains to be determined, but they must at least be a contributory factor to the observed changes in optical properties. It is notable, in this context, that the temperature interval of apparently negative optical retardation found for a (110) plate coincides almost exactly with the $\sim$797–817 K interval of irregular elastic softening and dissipation (data of Hayward *et al* 2005, reproduced in figure 8).

Hayward *et al* (2005) also investigated dielectric relaxation as a function of temperature and concluded that the observed electrical conductivity can be understood in terms of the mobility of oxygen vacancies. The relaxation times are greater than 10^{-8} s at all temperatures, however, and this aspect of the dynamics can probably be ruled out as a contributory factor to the central peak behaviour on a ps timescale.

7. Conclusions

Central peak effects have been found to influence markedly the $Pm\bar{3}m \leftrightarrow R\bar{3}c$ octahedral tilting phase transition in LaAlO₃. In particular, additional elastic softening beyond that expected on the basis of a fully calibrated Landau strain/order parameter coupling model clearly correlates with the appearance of the central peak in Brillouin spectra and the central peak itself disappears abruptly at the $Pm\bar{3}m \leftrightarrow R\bar{3}c$ transition point. This influence extends to at least $\sim$100 K below T_c and is

unlikely, therefore, to be due to critical fluctuations. Relaxation times of $\sim$10–100 ps, estimated from the width of the central peak, are consistent with a phonon timescale. On the basis of the simplest possible fitting of the spectra, two different relaxation processes have been postulated. Phonon density fluctuations could be intrinsic over a wide temperature interval while the possible flip mode, in the $\sim$20 K interval below T_c, also shows some dependence on microstructure.

The focus of this study has been on properties which depend on second derivatives of free energy, i.e. on susceptibilities. In this context, the anomalous elastic softening and the evolution of the soft optic modes are expected to be closely related. A semi-quantitative description of this interdependence has been provided in terms of the effective renormalization of the fourth order Landau coefficients b and b'. The implication is that the central peak mode couples also with E_g and A_{1g} soft modes though the strength of coupling with each is different. Raman spectra shown in figure 22 of Hayward *et al* (2005) show high intensity at low frequencies which could also be permissive of quasi-elastic scattering. If this is the case, at least part of the observed soft mode softening would be attributed to coupling with the central peak mode(s). A full mode–mode coupling model is likely to show that the soft mode frequencies remain low but finite, since there is no evidence for any breaks in symmetry at $\sim$760 or $\sim$805 K where linear extrapolations of ω^2 values would go to zero.

Calculations of elastic softening made using a constant value of the combined fourth order Landau coefficient ($3b^* + b'^*$) allow the equilibrium evolution of the order parameter to remain the same even under the influence of increasing contributions to the dynamics of the structure from the central peak mode. This is clearly only an approximation but is consistent with the temperature dependence of the available spontaneous strain data and the fact that there is no evidence for a tetragonal structure becoming stable, as would be predicted for $b'^* < 0$. If b'^* becomes smaller by the effect of coupling of acoustic modes with the phonon density fluctuations as $T \to T_c$, flipping of the octahedral tilt axis between $\langle 111 \rangle$, $\langle 011 \rangle$ and $\langle 001 \rangle$ would be increasingly favoured. The combined Brillouin and microstructural evidence is for a dynamical structure in the 20 K interval below T_c which appears to be cubic on a phonon length scale but still retains rhombohedral twins on a mesoscopic length scale.

LaAlO$_3$, together with SrTiO$_3$, has been an iconic material in the history of investigations of structural phase transitions in perovskites. The question then arises as to whether the new phenomena reported here occur only in LaAlO$_3$ or are typical properties of phase transitions in perovskites more generally. Hayward *et al* (2005) showed that there is evidence for a similar anomaly in the evolution of structural parameters in other aluminate perovskites, comparable with those that occur at $\sim$730 K in LaAlO$_3$. There is no reason to suppose that this is due to anything other than the same physical mechanism as in LaAlO$_3$ but further work is required to confirm that central peak modes exist more widely. Perhaps of more immediate interest is the possibility that other physical properties of these materials will also show marked anomalies in a relatively wide temperature interval below their transition

points. For example, diffusion coefficients might be modified by the degree of dynamical disorder in the flip mode interval such that trace elements could be introduced or engineered to control the development of tweed or twin microstructures, with implications for mechanical, electrical and chemical properties at lower temperatures.

Acknowledgments

References

Axe J D, Shirane G and Müller K A 1969 *Phys. Rev.* **183** 820–3

Birgeneau R J, Kjems J K, Shirane G and Van Uitert L G 1974 *Phys. Rev.* B **10** 2512–34

Bouvier P and Kreisel J 2002 *J. Phys.: Condens. Matter* **14** 3981–91

Bueble S, Knorr K, Brecht E and Schmahl W W 1998 *Surf. Sci.* **400** 345–55

Carpenter M A 2007 *Am. Mineral.* **92** 309–27

Carpenter M A, Becerro A I and Seifert F 2001 *Am. Mineral.* **86** 348–63

Carpenter M A, Buckley A, Taylor P A and Darling T W 2010a *J. Phys.: Condens. Matter* **22** 035405

Carpenter M A, Meyer H-W, Sondergeld P, Marion S and Knight K S 2003 *Am. Mineral.* **88** 534–46

Carpenter M A, Sinogeikin S V, Bass J D, Lakshtanov D L and Jacobsen S D 2010b *J. Phys.: Condens. Matter* **22** 035403

Chakoumakos B C, Schlom D G, Urbanik M and Luine J 1998 *J. Appl. Phys.* **83** 1979–82

Chrosch J and Salje E K H 1999 *J. Appl. Phys.* **85** 722–7

Cochran W and Zia A 1968 *Phys. Status Solidi* **25** 273–83

Coombs G J and Cowley R A 1973 *J. Phys. C: Solid State Phys.* **6** 121–42

Cowley R A 1996 *Phil. Trans. R. Soc.* A **354** 2799–814

Cowley R A and Coombs G J 1973 *J. Phys. C: Solid State Phys.* **6** 143–57

Darlington C N W 1997 *Phys. Status Solidi* b **203** 73–8

Fan H J, Kuok M H, Ng S C, Yasuda N, Ohwa H, Iwata M, Orihara H and Ishibashi Y 2002 *J. Appl. Phys.* **91** 2262–6

Feder J and Pytte E 1970 *Phys. Rev.* B **1** 4803–10

Fleury P A and Lyons K B 1979 *Solid State Commun.* **32** 103–9

Fleury P A and Lyons K B 1981 *Top. Curr. Phys.* **23** 9–92

Fleury P A and Lyons K B 1983 *Light Scattering Near Phase Transitions* ed H J Cummins and A P Levanyuk (Amsterdam: North-Holland) p 449

Geller S and Bala V B 1956 *Acta Crystallogr.* **9** 1019–25

Geller S and Raccah P M 1970 *Phys. Rev.* B **2** 1167–72

Harley R T, Hayes W, Perry A M and Smith S R P 1973 *J. Phys. C: Solid State Phys.* **6** 2382–400

Harrison R J and Redfern S A T 2002 *Phys. Earth Planet. Int.* **134** 253–72

Harrison R J, Redfern S A T, Buckley A and Salje E K H 2004a *J. Appl. Phys.* **95** 1706–17

Harrison R J, Redfern S A T and Salje E K H 2004b *Phys. Rev.* B **69** 144101

Hayward S A, Morrison F D, Redfern S A T, Salje E K H, Scott J F, Knight K S, Tarantino S, Glazer A M, Shuvaeva V, Daniel P, Zhang M and Carpenter M A 2005 *Phys. Rev.* B **72** 054110

Hayward S A, Redfern S A T and Salje E K H 2002 *J. Phys.: Condens. Matter* **14** 10131–44

Hellwig H, Hemley R J and Cohen R E 2003 *Fundamental Physics of Ferroelectrics 2003*; *AIP Conf. Proc.* **677** 65–73

Howard C J, Kennedy B J and Chakoumakos B C 2000 *J. Phys.: Condens. Matter* **12** 349–65

Howard C J and Stokes H T 1998 *Acta Crystallogr.* B **54** 782–9

Hushur A, Gvasaliya S, Roessli B, Lushnikov S and Kojima S 2007 *Phys. Rev.* B **76** 064104

Hushur A, Shigematsu H, Akishige Y and Kojima S 2005 *Appl. Phys. Lett.* **86** 112903

Ishidate T and Isonuma T 1992 *Ferroelectrics* **137** 45–52

Jackson J M, Sinogeikin S V and Bass J D 2000 *Am. Mineral.* **85** 296–303

Jiang F M, Ko J-H and Kojima S 2002 *Phys. Rev.* B **66** 184301

Jiang F M and Kojima S 2000a *Japan. J. Appl. Phys.* **39** 5704–10

Jiang F M and Kojima S 2000b *Phys. Rev.* B **62** 8572–5

Katiyar R S, Ryan J F and Scott J F 1971 *Phys. Rev.* B **4** 2635–8

Kim D H, Kojima S and Ko J-H 2005 *J. Korean Phys. Soc.* **46** 131–3

Kjems J K, Shirane G, Müller K A and Scheel H J 1973 *Phys. Rev.* B **8** 1119–24

Ko J-H, Kim D H and Kojima S 2006a *J. Korean Phys. Soc.* **49** S536–9

Ko J-H, Kim D H and Kojima S 2006b *J. Electroceram.* **17** 515–8

Ko J-H, Kim D H and Kojima S 2007a *J. Korean Phys. Soc.* **51** S67–70

Ko J-H, Kim D H and Kojima S 2007b *J. Korean Phys. Soc.* **51** 706–9

Ko J-H, Kim D H, Kojima S, Chen W and Ye Z-G 2006c *J. Appl. Phys.* **100** 066106

Ko J-H and Kojima S 2007 *Appl. Phys. Lett.* **91** 082903

Kuzel P, Dvorák V and Moch P 1994 *Phys. Rev.* B **49** 6563–74

Landau L D and Khalatnikov I M 1954 *Dokl. Akad. Nauk SSSR* **96** 469–72

Lehnert H, Boysen H, Schneider J, Frey F, Hohlwein D, Radaelli P and Ehrenberg H 2000 *Z. Kristallogr.* **215** 536–41

Lyons K B and Fleury P A 1977 *Solid State Commun.* **23** 477–80

Mączka M, Hanuza J and Kojima S 2008 *Phys. Rev.* B **77** 104116

Meyer H-W, Carpenter M A, Graeme-Barber A, Sondergeld P and Schranz W 2000 *Eur. J. Miner.* **12** 1139–50

Meyer H-W, Marion S, Sondergeld P, Carpenter M A, Knight K S, Redfern S A T and Dove M T 2001 *Am. Mineral.* **86** 566–77

Müller K A, Berlinger W and Waldner F 1968 *Phys. Rev. Lett.* **21** 814–7

O'Bryan H M, Gallagher P K, Berkstresser G W and Brandle C D 1990 *J. Mater. Res.* **5** 183–9

Oliver W F, Scott J F, Lee S and Lindsay S 1988 *Laser Optics of Condensed Matter* ed J L Birman, H Z Cummins and A A Kaplyanski (New York: Plenum) p 263

Oliver W F, Scott J F, Lee S A and Lindsay S M 1990 *J. Phys.: Condens. Matter* **2** 2465–71

Palko J W, Sayir A, Sinogeikin S V, Kriven W M and Bass J D 2002 *J. Am. Ceram. Soc.* **85** 2005–12

Pérez-Mato J M and Salje E K H 2001 *Phil. Mag. Lett.* **81** 885–91

Pytte E and Feder J 1969 *Phys. Rev.* **187** 1077–88

Rehwald W 1973 *Adv. Phys.* **22** 721–55

Salje E, Devarajan V, Bismayer U and Guimaraes D M C 1983 *J. Phys.: Condens. Matter* **16** 5233–43

Salje E K H, Gallardo M C, Jiménez J, Romero F J and del Cerro J 1998 *J. Phys.: Condens. Matter* **10** 5535–43

Salje E K H, Wruck B and Thomas H 1991 *Z. Phys.* B **82** 399–404

Schilling F R, Sinogeikin S V and Bass J D 2003a *Phys. Earth Planet. Int.* **136** 107–18

Schilling F R, Sinogeikin S V, Hauser M and Bass J D 2003b *J. Geophys. Res.* **108** 2304

Scott J F 1969 *Phys. Rev.* **183** 823–5

Scott J F and Oliver W F 1990 *Geometry and Thermodynamics—Common Problems of Quasi-Crystals, Liquid Crystals, and Incommensurate Systems* (*NATO ASI Series B* vol 229) ed J C Tolédano (New York: Plenum) p 453

Shabbir G, Ko J-H and Kojima S 2005 *Appl. Phys. Lett.* **86** 012908

Shabbir G and Kojima S 2004 *Ferroelectrics* **303** 167–71

Shabbir G and Kojima S 2007 *Appl. Phys. Lett.* **91** 062911

Sinogeikin S V, Jackson J M, O'Neill B, Palko J W and Bass J D 2000 *Rev. Sci. Instrum.* **71** 201–6

Siny I G, Husson E, Beny J M, Lushnikov S G, Rogacheva E A and Syrnikov P P 2001 *Physica* B **293** 382–9

Siny I G, Lushnikov S G and Katiyar R S 1997 *Phys. Rev.* B **56** 7962–6

Slonczewski J C and Thomas H 1970 *Phys. Rev.* B **1** 3599–608

Sokoloff J P, Chase L L and Boatner L A 1990 *Phys. Rev.* B **41** 2398–408

Sokoloff J P, Chase L L and Rytz D 1988 *Phys. Rev.* B **38** 597–605

Sondergeld P, Schranz W, Kityk A V, Carpenter M A and Libowitzky E 2000 *Phase Transit.* **71** 189–203

Stokes H T and Hatch D M 1988 *Isotropy Subgroups of the 230 Crystallographic Space Groups* (Singapore: World Scientific)

Thomas H and Müller K A 1968 *Phys. Rev. Lett.* **21** 1256–9

Tohei T, Kuwabara A, Yamamoto T, Oba F and Tanaka I 2005 *Phys. Rev. Lett.* **94** 035502

Tsukada S, Ike Y, Kano J, Sekiya T, Shimojo Y, Wang R and Kojima S 2006 *Appl. Phys. Lett.* **89** 212903

Tsukada S, Ike Y, Kano J, Sekiya T, Shimojo Y, Wang R and Kojima S 2007 *Japan. J. Appl. Phys.* **46** 7151–4

Tsukada S, Ike Y, Kano J, Sekiya T, Shimojo Y, Wang R and Kojima S 2008 *J. Phys. Soc. Japan* **77** 033707

Watt J P and Peselnik L 1980 *J. Appl. Phys.* **51** 1525–31

Yamaguchi M, Watanabe M, Inoue K, Akishige Y and Yagi T 1995 *Phys. Rev. Lett.* **75** 1399–402

Zhang M-S, Yagi T, Oliver W F and Scott J F 1986 *Phys. Rev.* B **33** 1381–5

Zhao J, Ross N L and Angel R J 2004 *J. Phys.: Condens. Matter* **16** 8763–73